Geomorphology 372 (2021) 107431

Contents lists available at ScienceDirect

Geomorphology

journal homepage: www.elsevier.com/locate/geomorph

Evolution of stony debris flows in laboratory experiments

Ivo Baselt [a,*], Gustavo Queiroz de Oliveira [a], Jan-Thomas Fischer [b], Shiva P. Pudasaini [c,d]

[a] *Chair of Hydromechanics and Hydraulic Engineering, Universität der Bundeswehr München, W.-Heisenberg-Weg 39, D-85579 Neubiberg, Germany*
[b] *Department of Natural Hazards, Austrian Research Centre for Forests, Rennweg 1, A-6020 Innsbruck, Austria*
[c] *Institute of Geosciences, Geophysics Section, University of Bonn, Meckenheimer Allee 176, D-53115 Bonn, Germany*
[d] *Chair of Landslide Research, Technical University of Munich, Arcisstrasse 21, D-80333 Munich, Germany*

ARTICLE INFO

Article history:
Received 19 January 2020
Received in revised form 21 August 2020
Accepted 14 September 2020
Available online 9 October 2020

Keywords:
Laboratory experiments
Landslide-induced stony debris flow
Flow evolution
Particle-fluid mixture flow
Flow architecture
Flow-like mass movements
Debris flood
Hyperconcentrated flow
Non-liquefied debris flow

ABSTRACT

The run out and destructive potential of gravitational multi-phase flows is largely determined by the mixture composition, the material properties of the solid particles and the fluid. One instrument to expand the understanding of the governing processes of flow is laboratory experiments. In this study, we concentrate experimentally on landslide-induced stony debris flows as a particular type of flow-like mass movement. We aim to observe different natural flow types for varying initial and boundary conditions. In a laboratory flume, 12.0 m long, 1.3 m wide and 0.3 m deep, we initiate stony debris flows and measured flow variables such as flow depth, mass, bulk density, front velocity and front shape for varying particle size, solid volume fraction and basal roughness. Our experimental results reveal that flow type and evolution changes significantly for different solid volume fractions, as well as for different basal roughness. The particle size had a noticeable effect on flow velocity and front shape. The smooth surface facilitated rapid, shallow, and turbulent flows. In contrast, experiments with rough beds showed relatively lower velocities and dense flow behaviour. Although the flow parameters covered only a small spectrum of the naturally possible parameter space, flow phenomena such as phase-separation, longitudinal sorting, steep front surges, or front overtopping were observed. We group our observed flows regarding the flow properties and classify them into common flow types: (1) debris flood (hyperconcentrated flow), (2) debris flow, and (3) non-liquefied debris flow. To compare our results with natural events and other experimental results, we analyse the data with several dimensionless numbers. The flows were generally dominated by grain collision on the smooth surface. Naturally, frictional forces gain more influence on the rough surface but did not overrule collisional forces. Viscous forces played only a minor role in our experiments, due to the lack of highly viscous fluid. Overall, we infer, that our well-controlled experiments mimicked natural stony debris flow and give new profound insights into the causal relationship of how the initial and boundary conditions affect the flow evolution.

1. Introduction

Debris flows are gravity-driven mass movements and appear as a mixture of fluid and solid particles. Because of the sudden occurrence, these events are often very difficult to predict, so is their geomorphic impact and hazard potential on humans and infrastructure (Egli, 1996). In general, a debris flow can occur if precipitation generates a runoff over a debris deposit and loose bed sediment is entrained and dispersed through the flow depth. Or, the debris flow is landslide-induced, where a compact sediment mass failure generates a downslope motion of a particle-fluid mixture. One of the most challenging aspects of understanding multiphase debris flow behaviour is the variety of alterable flow parameters and their intrinsic interactions. To depict debris flow properly, simulation tools nowadays partly built on multi-phase models (Pudasaini, 2012; Kowalski and McElwaine, 2013; Pudasaini and Mergili, 2019), which include several aspects of the two-phase and multi-phase particle-fluid flows as well as a large number of corresponding parameters and dynamical variables. Parameter estimate for simulation and prediction are, however, largely based on ad hoc assumptions and back calculations (Ancey et al., 2003; Mergili et al., 2017, 2020). Thus, the results appear to be highly sensitive to changes in initial and material conditions (Hussin et al., 2012; Frank et al., 2015; Gregoretti et al., 2019), resulting in an outright different characteristic of the flow and deposition (Mergili et al., 2018a, 2020).

Experimental investigations provide the essential opportunity to study the flow under controlled laboratory conditions and inspire new modelling methods (Turnbull et al., 2015). The data are crucial to validate and calibrate numerical approaches. With detailed knowledge about the initial and boundary conditions, experimental debris flows can gain important physical insights into complex processes. However, these laboratory experiments often suffer from scale effects that make

---

[*] Corresponding author.
E-mail address: ivo.baselt@unibw.de (I. Baselt).

https://doi.org/10.1016/j.geomorph.2020.107431
0169-555X/

the comparison of specific dimensionless numbers for geometric and dynamic similarity inevitable. Many results of laboratory experiments with well-known conditions and parameters had been presented over the years. The experimental setups were predominantly in straight rectangular flumes on a sub-meter to meter-scale (Hungr and Morgenstern, 1984; van Steijn and Coutard, 1989; Egashira et al., 2001; Parsons et al., 2001; Sanvitale et al., 2011; Cageao, 2014; de Haas et al., 2015; Lyu et al., 2017; Cheng et al., 2019). Other experiments had been conducted in rotating flumes or geotechnical centrifuges, in particular to gain steady flow conditions (Kailey et al., 2011; Kaitna et al., 2011; Hotta, 2011; Gray, 2018). In some investigations, the physical parameters had been assumed to be idealised like artificial glass or PVC balls as a substitute of natural grains (Larcher et al., 2007; Armanini et al., 2008; Hsu et al., 2011; Hotta, 2011; Rondon et al., 2011; Turnbull et al., 2015; Gray, 2018; Cheng et al., 2019). Larger-scale, quasi two- and three-dimensional experiments provide experimental benchmarks and have achieved deep insights into debris flow characteristics (Major, 1997, 1998; Iverson and LaHusen, 1989; Lanzoni, 1993; Tognacca, 1999; Denlinger and Iverson, 2001; Iverson et al., 2004, 2010; Reid et al., 2011; Armanini, 2015; Scheidl et al., 2015; McFall et al., 2018; Wang et al., 2018). Laboratory experiments allow studying natural flow behaviour like phase-separation (Pudasaini and Fischer, 2020b), grain sorting, or the alternating process of erosion and deposition (Pudasaini and Fischer, 2020a) under predefined, controlled conditions. Typical initial and boundary conditions include solid volume fraction, sediment composition, basal roughness, and bed slope. Additionally to induce different flow velocities and observe different flow characteristics, the bed slope was often varied. Lanzoni et al. (2017) aimed to better clarify the role of quasi-static and collisional stresses in determining the velocity profile that establishes within the body of a coarse-grained debris flow flowing over an erodible bed in different bed slopes. Based on the experiments of Lanzoni (1993) under different bed slopes and variable sizes of artificial grains, Lanzoni et al. (2017) conclude, that sediment size, more than water discharge, likely controls the flow depth and the sediment concentration.

Nevertheless, the amount of water has a major influence on flow velocity and overall flow dynamics. Even if granular solids are closely packed in natural and artificial environments, they feature interstitial pore space, which can partly or fully be filled by liquid (Iverson and LaHusen, 1989). Natural debris flow events have been reported with different solid volume fractions varying between 14% to 75% water by volume (Costa, 1984; Mergili et al., 2018a, 2018b). Savage (1994) mentions solid volume fractions between 0.3 and 0.6 for flowing bulk solids. Fleischer (2012) complemented Costa's overview (Costa, 1984) of how to distinguish debris flows from debris floods and torrential flows regarding the solid volume fraction. Whereas debris floods may reach a maximum solid volume fraction of 0.4, in debris flows that can be exceeded until 0.7–0.9 (Fleischer, 2012), but usually, the solid volume fraction ranges between 0.25 and 0.86 (Costa, 1984). With sufficient water, the rapid flow may disperse grains throughout the whole depth (Takahashi, 1983), which is also influenced by the bed slope (Lanzoni et al., 2017). High dilute torrential floods, with extremely low solid volume fraction, transport mostly fine sediment in relatively small quantities compared to total flow volume. Very high values of the solid volume fraction lead to almost dry granular flows. The spectrum in-between (flow transport more volume of sediment than water) (Pierson, 2005; Pudasaini, 2012; Pudasaini and Mergili, 2019) can range from dense sliding masses, inertial debris flow, dilute flows, muddy-viscous debris or hyperconcentrated mixtures.

Besides bed slope and water content, variations in basal roughness and grain size have been studied. Iverson et al. (2010); de Haas et al. (2015) found out, that the water content and the presence of fine particles influence the flow and the deposition significantly. Fine content influences the viscosity of the fluid phase and therefore the rheology of the flow mixture (Pudasaini and Mergili, 2019). On the contrary, the size of the grains played a minor role (de Haas et al., 2015). If a channel bed in mountain regions, which is mainly composed by gravel, and fine cohesive particles are absent, is mobilized, the fluid properties in such stony debris flows are close to water and the flow dynamics is essentially dominated by grain collision (Costa, 1984; Gregoretti et al., 2019). Savage (1994) defines such particle-fluid flow as an assembly of discrete solid components dispersed in a fluid, in which direct interactions between the individual solid constituents are frequent. But also other grain supporting mechanism such as buoyancy, cohesion and yield strength of the suspension material occur (Hampton, 1979; Pudasaini and Mergili, 2019). Some experimental studies concentrated on such coarse-grained stony debris flows or non-cohesive sediments, respectively (Lanzoni, 1993; Mainali and Rajaratnam, 1994; Garcia Aragon, 1995; Armanini et al., 2005; Deangeli, 2008; Armanini, 2015; Stancanelli et al., 2015).

Depending on the specific value of a selected parameter or parameter combinations in laboratory experiments, the moving multi-phase mixtures may evolve differently. For natural events, common types of flow-like mass movements are classified according to their individual flow attributes (Varnes, 1978; Hutchinson, 1988; Hungr et al., 2001, 2014), expressed e.g. in characteristic lateral and longitudinal profiles, flow velocities, front shapes, spatial grain distribution, and overall flow dynamics. According to Hungr et al. (2001), the following classes of flow types can be distinguished: dry (or non-liquefied) sand (silt, gravel, debris) flow; sand (silt, debris, weak rock) flow slide; clay flow slide; peat flow; earth flow; debris flow; mud flow; debris flood or hyperconcentrated flow (Pierson, 2005); debris avalanche; and rock avalanche.

In laboratory experiments, the flow could either be assigned to one of these classifications or had at least some properties of such flow types. For example, Iverson et al. (2010) observed flows with a coarse-grained debris front and a relatively more diluted body following behind as a result of phase-separation (Pudasaini and Fischer, 2020b) during motion. Such phenomena is an often observed example in a natural debris flows (Stiny, 1910; Pierson, 1986; Takahashi, 1991) and is called head-body structure and sometimes summarised figuratively as a flow architecture (Turnbull et al., 2015). The debris flow can also be divided into multiple travelling fronts and roll waves, in which subsequent surges can run faster and sometimes overtop the previous fronts (Bryant, 2005; Arai et al., 2013; Turnbull et al., 2015). de Haas et al. (2015) studied the influence of fine sediment intensively, reporting flows, which can be addressed as clay flow slide or mud flow. Dry (or non-liquefied) granular flows, as a flow-like movement of loose dry or moist, sorted or unsorted granular sediment, without significant excess pore-pressure (Hungr et al., 2001) are described, e.g., in Lanzoni (1993); Mainali and Rajaratnam (1994); Garcia Aragon (1995); Armanini et al. (2005); Deangeli (2008); and Armanini (2015). Debris floods are described by Pierson (2005), who named it hyperconcentrated flow, where the flow shows properties between fluvial flow and debris flow. This highly rapid and turbulent surging flow of water, heavily charged with debris (Hungr et al., 2001), evolve differently from non-Newtonian flow and do not show typical phenomena of debris flows, such as levees or prominent phase-separation. Hyperconcentrated flows show strong turbulence and a steep water-surface slope, often describes as fast-moving "wall" (Pierson, 2005).

Overall, laboratory experiments described in the literature were conducted under a relatively high variability of initial and boundary conditions. Varying the bed slope highly influences the flow dynamics and might suppress the observability of more sensitive parameters (e.g. particle size). Besides, former experiments were often conducted under a wide spectrum of particle sizes and grain distributions. This also included fine particles, muddy components, or viscous slurry. Depending on the step size of the investigated grain sizes and the amount of fine content, different flow types occurred, but were often superimposed by collisional, viscous, and frictional stresses. Moreover, the value of the solid volume fraction distinctively determines the flow dynamics, because it can also range in a wide spectrum and let the flow differ between a slow crawling mass and high turbulent water flow with suspended sediment.

In the presented work we explore the range and identify the occurrence of natural flow types (Hungr et al., 2001; Pierson, 2005) characterised by prominent flow depth, flow velocity, front shape, characteristic lateral and longitudinal profiles, spatial grain distribution for a fixed experimental setup with a predefined spectrum of initial and boundary conditions. Therefore, we were particularly interested in landslide-induced stony debris flows, where a mixture of natural coarse sediments without fine cohesive components and pure water is suddenly released from a reservoir and moves down a flume with a fixed slope. Such scenarios can also occur in runoff-generated debris flows, where local low-gradient sections of the channel act as sediment capacitors and the accumulated temporary stored sediment is released periodically as debris flow surges (Kean et al., 2013). Those flows are classified hierarchically as gravitational mass movements - subaerial mass movement - debris flow - stony-type debris flow (Takahashi, 2014). Prototypes for our investigated flows are existing field sites with a coarse-grain matrix (e.g. summarised in Lanzoni et al. (2017), Table 2 or reported by Bernard et al. (2019)), where the density and the viscosity of the interstitial fluid are close to pure water and the solid volume fraction range between 0.3 and 0.6. The slopes at these sites range between 9° and 20°.

By studying those flows under laboratory conditions, we, firstly, aim to deepen the knowledge about coarse-grained particle-fluid mixture flows as a niche of debris flow. Secondly, the work shall provide new extensive data set from well-controlled laboratory experiments for the calibration and validation purpose of computational multi-phase mass flow models (Pudasaini and Mergili, 2019). To study the grain size influence, we used a fixed bed, so that no entrainment occurs and might change the grain size distribution. However, to investigate bed friction, the experiments were conducted on smooth or rough basal conditions. Nevertheless, the flow could be additionally governed by other morphodynamic mechanisms, which actually cannot be observed during the experiment but might act locally in the mixture column. For example, the interstitial fluid can lubricate the contact area between grains or between grains and the bed. Therefore, we calculate several relevant dimensionless numbers to determine the acting flow regimes to reveal dominating stresses in the flow and discuss the transferability to natural events and other experimental data.

To investigate the possible flow types in our experimental setup we structured the paper as follows. The second section explains our experimental setup and the used measurement devices as well as discusses the measurement accuracy and reproducibility. In Section 3, we itemise the most important dimensionless numbers for our field of interest and name typical values of natural events and other experiments. After that, we present the results and outcomes from 72 experiments in Section 4 regarding the flow depth, the normal force (mass), the depth-averaged bulk density, the front velocity and the shape of the debris front with varying particle sizes, basal roughness and solid volume fractions. In Section 5, we use the dimensionless numbers from Section 3 to evaluate and classify our stony debris flows. The calculation of relevant dimensionless numbers reveals that the overall flow regime is dominated by collisional forces. However, in some subsets, the frictional force gains some influence. In Section 6, we discuss our experimental findings and explain why we assign the observed flows to the categories of natural flow-like mass movements: (1) debris flood (hyperconcentrated flow), (2) debris flow with head-body architecture, and (3) non-liquefied debris flow. We argue, that these flow types were essentially dictated by basal roughness and solid volume fraction in our experiments, which had a ripple effect on flow depth and front velocity. The particle size is the main player of the shape and the evolution of the front geometry. We reclaim our research question in the conclusion and summarise our major experimental findings. Even if we only observed bulk flow behaviour in a limited parameter spectrum, we infer that our laboratory experiments mirror the overall flow characteristic of natural stony debris flow events.

2. Experimental setup, materials and methods

2.1. Flume setup

We conducted 72 experiments in a laboratory flume to investigate the complex dynamic behaviour of particle-fluid mixtures. The experiments were operated in the Laboratory for Hydromechanics and Hydraulic Engineering at the Universität der Bundeswehr München. We converted a hydraulic channel, 12.0 m long, 1.3 m wide and 0.3 m deep, into a geomorphological flume, which has a rectangular cross-section of 0.39 m^2 (Fig. 1). Similarly to other experimental flumes setups a change in bed slope appears rather complicated (e.g. due to geometry, work safety, costs). So, the bed slope was limited in our setup to 19.1°. A prismatic reservoir in the upper part of the flume stored the unsorted water-saturated sediment. A flap, mounted at the lower end of the reservoir, was used as a headgate system to detain the particle-fluid mixture before its release. The flap had a cross-section of 50 cm wide and 15 cm high. In this setup, the reservoir opening width appears to be narrower than the flume itself and was located in the centre of the top of the flume. Therefore, a fully three-dimensional flow developed by enabling lateral debris flow expansion. Deflection walls were placed close to the reservoir outflow to avoid brusque lateral shocks of the debris material during the release. All longitudinal lengths are measured from the reservoir exit, reaching a horizontal runout plane at 6.7 m with an area of 3.5 m length and 3.67 m width. Variations in the basal friction were realised by considering two bottom surfaces with different roughness. Half of the experiments were performed with a smooth surface, represented by varnished wooden plates with a minimised basal friction effect. The other half were performed on a rough basal surface, increasing the surface roughness by spreading a mixture of about 3 mm sand and waterproofed glue on separate plates and mounting them upon the bottom surface (similar to Hungr and Morgenstern (1984)). The achieved effective basal roughness was of approximately 1.5 mm and hence laid in the range of the smallest particle diameter of the debris sediment. Thus, friction effects would be comparable relevant than particle collisional effects and lubrication effect due to the water content in the particle-fluid mixture during downhill moving.

2.2. Measurement techniques, accuracy and reproducibility

Ultrasonic transducers, miniature load cells and one digital video camera were utilised to measure the evolution of flow depth, basal normal force, velocity and shape of the debris front. The ultrasonic transducers (Siemens SonarBero 3RG) measured the space-time evolution of the debris flow depth by evaluating the elapsed times between the emitted and reflected pulses with a frequency of 50 Hz. The load cells (C9C 50 N Hottinger Baldwin Messtechnik) working as pressure sensors measured basal normal force by taking into account the slope effect. A single load cell was mounted with a circular PVC-plate of 7 cm diameter before both were fixed into an assembled PVC-box, which was later countersunk into the bed. An apropos top lid opening was sealed with a thin rubber film to prevent the cell from intruding sediment (similar as in Bernard et al. (2019)). Each ultrasonic transducer formed together with one pressure device a single measurement location, of which eight were arranged along the flume in four cross-sections at 1.75 m, 3.00 m, 4.25 m, and 5.50 m from the reservoir exit (Fig. 2A, Fig. 2B). The measuring position were arranged along the centre line (S1C, S2C, S3C, S4C) and additional ultrasonic transducers and load cells aside from the centre line to observe the lateral expansion of the debris flow (S3L, S2L, S3R, S2R). We recorded separate hydrographs in four measurement spots located in the second cross-section on the left side (S2L) and the right side (S2R) and in third cross-section (S3L, S3R), respectively. Each sensor had an equal distance of 0.42 m to the centre devices on both sides. In addition, a high-speed digital video camera (Basler CMOSIS ACA2000-340KC) captured detailed evolution of the debris flow front from release to deposition with a nominal rate of 50 frames per second. To assess the

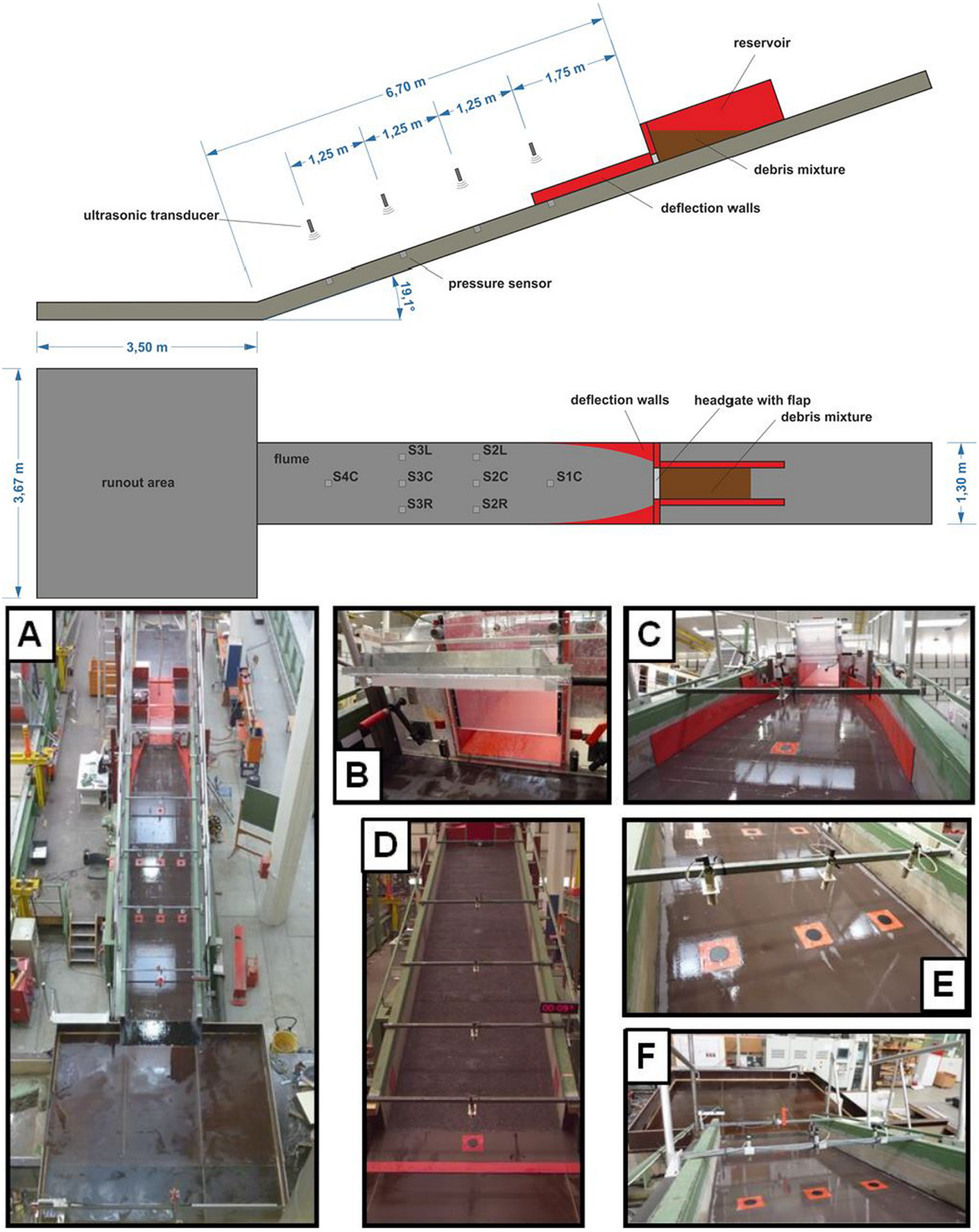

Fig. 1. Top panels: Dimensions and geometry of the experimental flume and the locations of the initial debris and the measurement devices. Bottom panels: A detailed overview of the flume: (A) The full view of the laboratory flume with a smooth surface. (B) Reservoir with flap system. (C) The up view of the flume close to the release area with installed deflection walls. (D) Flume with a rough surface. (E) Location of ultrasonic transducers and pressure sensors. (F) The end of the flume and the runout plane.

flow velocity and front shape, post-processing was performed using an image analysis technique, which provides a peculiar signal when pixel reflectance changed while debris material was overflowing the bed (De Oliveira et al., 2015). Our analysis tracked the signal and clearly defined the debris front in each image frame. All measurement devices had been synchronized with data acquisition of 50 Hz including a digital time signal triggered simultaneously with reservoir flap opening.

For a single measurement, the ultrasonic transducers achieve an accuracy of ±0.5 mm and the load cells of ±0.1 N. The ultrasonic data acquisition is indirect and immediate, which was appropriate in all experiments. In contrast, the load cells measured the debris mass in direct contact but exhibited more inert behaviour. While debris had been flowing over the load cells, a perceivable time delay between mass appearance over the sensor and data acquisition occurred. Unfortunately, streamflows over the smooth bed had been usually too fast to assign received data to the associated time signal properly. For all flows over the rough bed, the time delay was negligible. Thus, we managed to combine data from each ultrasonic transducer and its corresponding load cell to investigate the bulk density (De Oliveira et al., 2016). The digital video camera provides a resolution of 2040 × 1086 pixels and was calibrated

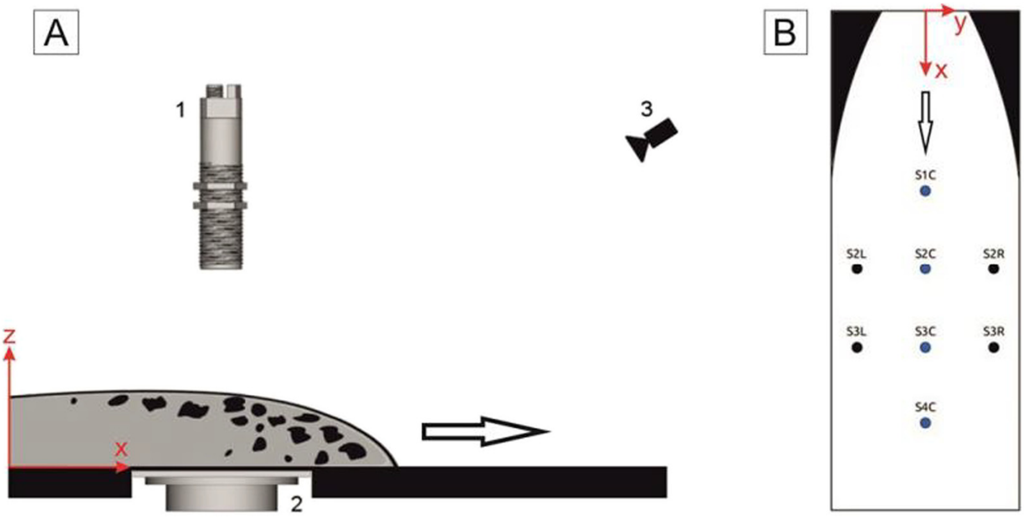

Fig. 2. Panel A shows a schematic side view of the measurement setup consisting of (1) an ultrasonic transducer, (2) a pressure sensor, and (3) a video camera (not to scale). Panel B displays the measurement locations P_{S1C}=(1.75 m, 0 m), P_{S2C}=(3.00 m, 0 m), P_{S3C}=(4.25 m, 0 m), P_{S4C}=(5.50 m, 0 m), P_{S2L}=(3.00 m, − 0.42 m), P_{S2R}=(3.00 m, 0.42 m), P_{S3L}=(4.25 m, − 0.42 m), P_{S3R}=(4.25 m, 0.42 m) along the flume with the flow in downstream direction indicated by the arrow. The sensors are named according to their position in the cross-sections (indicated by 1, 2, 3, 4) and whether they are placed at the centre line of the flume (indicated by C) or, left and right of the centre line (indicated by L or R).

with a checkerboard to correct the lens distortions and obtain physically correct and undistorted image pixels. We extracted the debris front position and the front shape from the images during the postprocessing by achieving an accuracy of 8 mm. We measured the time when the debris front overran a certain cross-section with a standard deviation over all repeated experiments of 0.07 s. Using the law of error propagation, the front velocity was determined with an accuracy of 0.05 m s^{-1}.

To account for the remaining experimental uncertainty (e.g. due to non controllable environmental variables), each experiment was repeated three times with the same initial and boundary conditions. After we had evaluated our results, we asserted that our experiments were repeatable. Therefore, we averaged the data from each triple and, for the sake of improved clarity, we will only present the mean values for the repeated experiments of flow depth, normal force, bulk density, front position over time, front velocity and front shape in the upcoming sections and figures.

2.3. Material properties and initial conditions

The initial composition of the particle-fluid mixture was varied with different particle sizes of natural nearly sphere-shaped grains of 1.34 mm ≤ d_{50} ≤ 5.84 mm. The solid material varies between different sizes of gravel and sand and is categorised within very fine, fine and coarse particles (Table 1). The sediments had been analysed accurately prior to the experiment (Fig. A14). The particle size was obtained by sieve analysis while densities had been analysed by using a gas pycnometer. Hydraulic conductivities were between $1 \cdot 10^{-4}$ m s^{-1} and $1 \cdot 10^{-3}$ m s^{-1} for a large sand fraction (0.63 mm ≤ d_{mean}<2 mm) and between $1 \cdot 10^{-3}$ m s^{-1} and $1 \cdot 10^{-2}$ m s^{-1} for a fine gravel fraction (2 mm ≤ d_{mean}<6.3 mm). We interpolated between these limits for our mean particle sizes to get the conductivity values. Tilt-table tests (Pudasaini and Hutter, 2007) had been conducted to determine basal friction angles for the three particle sizes on both smooth and rough bed. The physical properties of the sediments are in agreement with the typical values of other debris flow mixtures (Iverson, 1997).

To ensure the inter-comparability, especially with respect to the measured flow velocities, all experiments had the same initial mass, providing an equal potential energy throughout the experiments. In each experiment a mixture of 300 kg of unsorted particle-fluid mixture was stored in the reservoir. The initial volume of the solid varied between 157 l and 177 l depending on the desired solid volume fraction in the experimental subset. The stored sediment was saturated (with density and viscosity: ρ_{water}=1000 kg m^{-3}, $\mu \approx 0.001$ Pa s) to achieve four initial solid volume fractions in the reservoir α_s=[0.43; 0.47; 0.51; 0.55], which are in the range of natural conditions of the prototypes with coarse-grained particle-fluid mixture flows (Lanzoni et al. (2017), Table 2), but are also typical in other field sites or were used in former experimental and numerical investigations (Iverson, 1997; Pudasaini, 2012; de Haas et al., 2015; Mergili et al., 2018a, 2018b). We conducted experiments with α_s=0.55 only for the smooth surface. For the rough basal surface and α_s ≥ 0.55, the debris flows had either stopped instantly in the flume or had been moving just a bit due to poor basal lubrication and did not allow decent data evaluation. In comparison, solid volume fractions lower than 0.43 had often developed into slightly chaotic dilute flows, which reached the runout plane with high speeds, causing spraying and a significant loss of material.

All predefined homogeneous debris mixtures were in saturated conditions and the pore volume was completely filled with water. The bulk density of the released watered debris was determined as

$$\rho_{bulk} = \alpha_s \rho_{solid} + (1 - \alpha_s) \rho_{water} \tag{1}$$

with initial values between 1701 kg m^{-3} and 1902 kg m^{-3}. The hydraulic diffusivity was determined by $D = kn/(\mu C)$ (Iverson,

Table 1
Sediment and bed surface properties used in the experiments.

Particle size			Solid density of particle	Dry bulk density	Hydraulic conductivity	Internal friction angle	Basal friction angle	
Category (material)	d_{50} [mm]	d_{mean} [mm]	ρ_{solid} [kg m^{-3}]	ρ_{dry} [kg m^{-3}]	K [m s^{-1}]	ϕ [°]	Smooth δ [°]	Rough δ [°]
Coarse (gravel)	5.84	6.25	2630	1540	$1 \cdot 10^{-2}$	29.2	26.3	34.0
Fine (gravel)	2.29	2.54	2630	1540	$2 \cdot 10^{-3}$	28.2	26.8	33.6
Very fine (sand)	1.34	1.44	2640	1540	$6 \cdot 10^{-4}$	28.0	25.1	30.1

Table 2
Overview and a brief explanation of the dimensionless numbers used in this study. Detailed information including references as well as typical ranges in natural flows and other experiments are collated in Appendix C.

Number	Equation	Explanation
Pressure	$N_p = \frac{\sqrt{L/g}}{h^2/D}$	Relation between the timescale for downslope flow and pore pressure diffusion; $N_p \ll 1$ in most natural geophysical flows
Savage	$N_{Sav} = \frac{\rho_{solid}\dot{\gamma}^2 d_{mean}^2}{(\rho_{solid} - \rho_{water})gh \tan\phi \cos\theta}$	Ratio of grain collision stresses and gravitational grain contact stresses; flow dynamics is significantly affected by grain collision stresses if $N_{Sav} > 0.1$
Bagnold	$N_{Bag} = \left(\frac{\alpha_s^{1/3}}{(\alpha_{s,\,\max}{}^{1/3} - \alpha_s^{1/3})}\right)^{1/2} \frac{\rho_{solid}\dot{\gamma} d_{mean}^2}{\mu}$	Bagnold (1954): comparison of grain collision stresses and viscous fluid stresses; collisional dominated flow for $N_{Bag} > 450$
Friction	$N_{fric} = \frac{\alpha_s}{(1 - \alpha_s)} \frac{(\rho_{solid} - \rho_{water})gh \tan\phi \cos\theta}{\mu\dot{\gamma}}$	Quotient of frictional to viscous forces; friction dominated flows for $N_{fric} > 2000$
Mass	$N_{mass} = \frac{\alpha_s}{(1 - \alpha_s)} \frac{\rho_{solid}}{\rho_{water}}$	Ratio of solid inertia to fluid inertia; typically $1 \le N_{mass} \le 10$
Darcy	$N_{Dar} = \frac{\mu}{\alpha_s \rho_{solid} \dot{\gamma} k}$	Ability of pore fluid pressure to buffer grain interactions; typically $10^4 \le N_{Dar} \le 10^8$ in natural flows
Stokes	$N_{St} = \frac{1}{18} \frac{\rho_{solid}}{\rho_{water}} \frac{d_{mean}^2 \dot{\gamma}}{\nu}$	Ratio of the time scale of deceleration and the time of grain movement; viscous regime: $N_{St} \ll 1$, inertial regime: $N_{St} \gg \sqrt{\rho_{solid}/(\rho_{water} C_d)}$ and $\sqrt{\rho_{solid}/(\rho_{water} C_d)} \ll 1$, accelerated flow: $N_{St} \gg 1$
Froude	$Fr = \frac{v}{\sqrt{gh \cos\theta}}$	Ratio between the inertial and gravity forces; subcritical flow: $Fr < 1$, critical flow: $Fr = 1$, supercritical flow: $Fr > 1$
Reynolds	$Re = \frac{h\sqrt{gL}}{\mu/\rho_{bulk}}$	Classifies whether a flow is in laminar or turbulent conditions, typically $Re > 10^6$ in natural geophysical flows
Particle Reynolds	$Re_p = \frac{\rho_{water} d_{mean} v}{\mu}$	Opposes the effects of particle collision and pore fluid viscosity, ratio between the solid inertial stress and the fluid viscous stress; fluid start to show inertial effects with respect to the grains in the mixture for $Re_p > 1$

1997; Major, 2000; de Haas et al., 2015). Therein, the hydraulic permeability

$$k = \frac{K\mu}{\rho_{water} g}, \tag{2}$$

takes into account the hydraulic conductivity K according to the particle sizes (Table 1), the porosity $n = 1 - (\rho_{dry}/\rho_{solid}) \approx 0.42$, the dry bulk density ρ_{dry}, the true particle solid density ρ_{solid}, the dynamic fluid viscosity $\mu = \rho_{water}\nu$, the kinematic viscosity ν, the compressibility of pore fluid C, and the fluid density ρ_{water}. Furthermore, $g = 9.81\ \mathrm{m\,s^{-2}}$ is the gravitational acceleration. In our experiments, the hydraulic permeability ranged in the spectrum of $6.1 \cdot 10^{-11}\ \mathrm{m}^2 \le k \le 1.0 \cdot 10^{-9}\ \mathrm{m}^2$, which is in good agreement with various material in saturation and natural flows (Klute and Dirksen, 1990; Iverson, 1997; Major, 2000; Legros, 2002; Iverson, 2005). Because we had been omitting fine cohesive particles in our experiments, the solid volume fraction of fine particles, which would have been able to occupy fluid pore volume (Hampton, 1979), was inevitably zero. For this reason, the interstitial fluid viscosity μ was about the viscosity of pure water. We assumed almost negligible compressibility of the interstitial fluid, $C = 2 \cdot 10^{-9}\ \mathrm{Pa}^{-1}$ as for pure water. Indeed, our sediment was very permeable, what is expressed by a hydraulic diffusivity between 51 and 845 $\mathrm{m^2\ s^{-1}}$, which is higher than in natural debris sediments (Major, 2000).

3. Dimensionless characterisation

The dimensional analysis helps to gain insights into the flow physics, characterise the flow type, and provide a connection between experimental and natural flows. Laboratory data is typically limited by scaling problems (Iverson and LaHusen, 1993; Iverson, 2015) and thus, our simulated flow evolution will not be able to fully mimic the complex flow dynamics of a natural event due to limited geometric (flow depths are comparatively small) and dynamic scaling. To compare results from other experiments, as well as from field surveys, we will further analyse the measured data by calculating relevant dimensionless numbers (Table 2), which are explained in more detail including typical ranges in natural flows and other experiments in Appendix C. Our experiments will achieve dynamic similarity when the values of relevant dimensionless numbers range in those of natural flows. By evaluation of these numbers, the driving processes of the experimental flows, like grain collisions, viscous and turbulent shearing, and solid-fluid interactions are categorised. Interestingly, many of these non-dimensional numbers contain the solid volume fraction α_s. As α_s evolves during the flow, these non-dimensional numbers clearly indicate the importance of two-phase and multi-phase mass flow modelling (Pudasaini, 2012; Pudasaini and Mergili, 2019) to properly describe debris flow dynamics. To be consistent with the Coulomb friction force for the inclined slope, the Savage and Friction numbers should have included the factor cosθ emerging from the channel inclination, see, e.g., Pudasaini and Hutter (2007) and Pudasaini and Mergili (2019). However, in the previous considerations they appear without the factor cosθ. Here, we wrote them correctly that includes the factor cosθ, and all the corresponding non-dimensional numbers are calculated accordingly. This also applies to those numbers in the Appendix C.

4. Results and observations

After filling the reservoir with sediment and water, the headgate flap was triggered electronically and the data acquisition started simultaneously. Beginning with the opening of the headgate the stored water-saturated sediment faced the open downstream outflow area and began to abruptly disembark the reservoir, due to gravity and hydraulic pressure gradient. Following the research question, we evaluate the spatio-temporal evolution of flow variables with respect to varying initial conditions. Particular emphasis is given to the observation of possible properties of natural flow types, characterised by prominent flow depth, flow velocity, front shape, phase-separation, and head-body diversion. If observable, these should arise from the variation of basal roughness, solid volume fraction, and/or particle size. In the following, we present and describe data on quasi-steady conditions, in particular, occurred between measurement locations three and four. Subsets with unsteady conditions, relevant only in subsets with a smooth surface and $\alpha_s = 0.43$, are described in Appendix B. Figures for all subsets are available in the Supplementary resource.

4.1. Flow depth evolution

The ultrasonic transducers allow evaluating flow depths along the centre line and in the lateral direction. A selection of the hydrographs along the centre line is presented in Fig. 3. The first and second rows show the flow depth evolution on the smooth bottom surface. The first

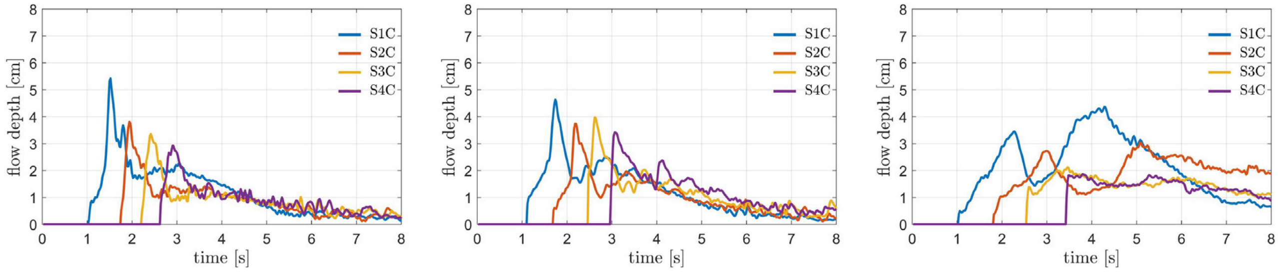

(a) smooth s., very fine particles, $\alpha_s = 0.47$ (b) smooth s., very fine particles, $\alpha_s = 0.51$ (c) smooth s., very fine particles, $\alpha_s = 0.55$

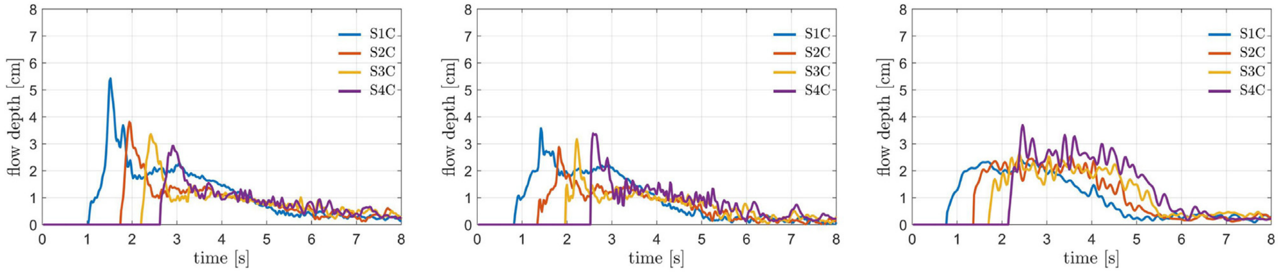

(d) smooth s., very fine particles, $\alpha_s = 0.47$ (e) smooth s., fine particles, $\alpha_s = 0.47$ (f) smooth s., coarse particles, $\alpha_s = 0.47$

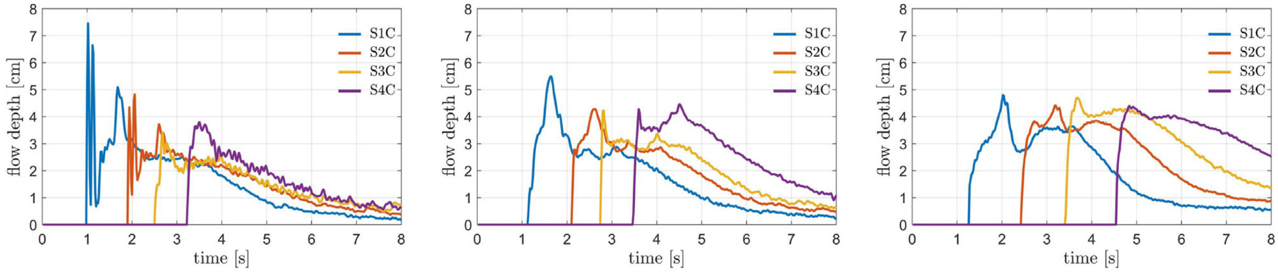

(g) rough s., fine particles, $\alpha_s = 0.43$ (h) rough s., fine particles, $\alpha_s = 0.47$ (i) rough s., fine particles, $\alpha_s = 0.51$

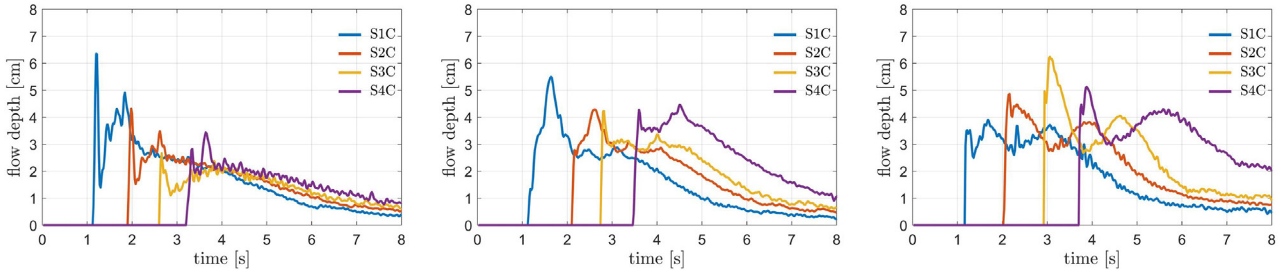

(j) rough s., very fine particles, $\alpha_s = 0.47$ (k) rough s., fine particles, $\alpha_s = 0.47$ (l) rough s., coarse particles, $\alpha_s = 0.47$

Fig. 3. Selection of flow depth measurements along the flume **centre line** in the downslope direction for quasi-steady conditions. Subsets that showed rather unsteady condition (smooth surface, α_s=0.43) are shown in Appendix B.

one concerns very fine particles for increasing solid volume fraction while the second one a constant solid volume fraction for increasing particle size. The third and fourth row are analogous to the previous rows but display exemplified data for flows over the rough surface for fine particles for increasing solid volume fraction (Fig. 3g–i) and for α_s=0.47 and increasing particle size (Fig. 3j–l). Figs. 4 and 5 display the data of the left, centre and right sensor of the second and third cross-section for the lateral hydrographs corresponding to the centre positions in Fig. 3.

4.1.1. Smooth surface

4.1.1.1. Equal particle size and varying solid volume fraction. The hydrographs for flows over the smooth surface are generally characterised by a rapid flow (Fig. 3 first and second row). The time the first sensor was triggered was around 1 s after the flap had been opened. So, the arrival was nearly independent of the initial solid volume fraction. However, the routing downstream of sensor S1C was influenced by the water content in the mixture with very fine particles. Higher solid volume fraction led to lower flow velocities in these cases (Fig. 3 first row). On the contrary, the triggering times for the sensors were rather independent of solid volume fraction in subsets with fine and coarse particles. The amount of water in the released mixture affected also the debris height, especially in subsets with very fine particles. In these cases, the hydrographs show steep and sharp debris fronts, which remained dominant in every sensor location even though peak height was diminished in lower sensor locations due to shearing and spreading of the flow (Fig. 3a, b). Following the moving front triggering S1C until S4C, the height difference of the front peaks became less significant the higher the solid volume

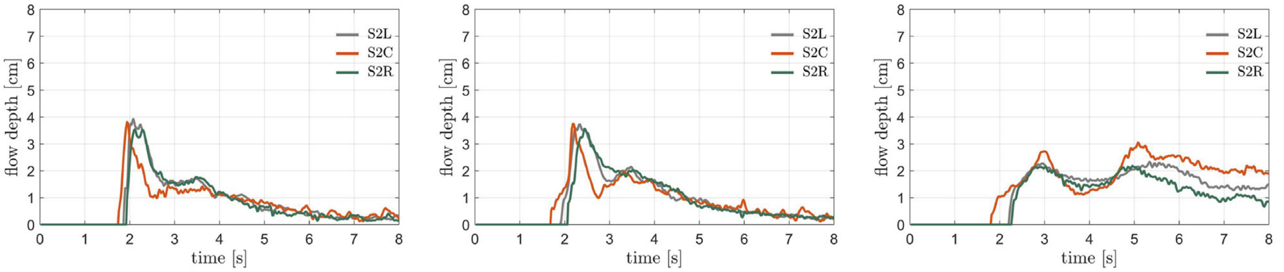

(a) smooth s., very fine particles, $\alpha_s = 0.47$ (b) smooth s., very fine particles, $\alpha_s = 0.51$ (c) smooth s., very fine particles, $\alpha_s = 0.55$

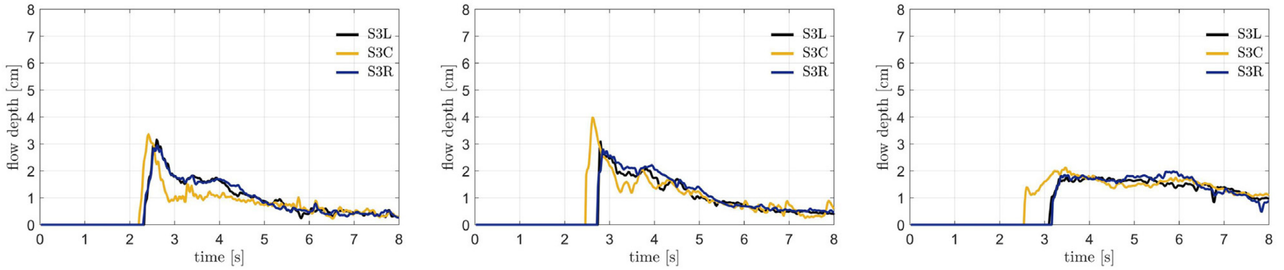

(d) smooth s., very fine particles, $\alpha_s = 0.47$ (e) smooth s., very fine particles, $\alpha_s = 0.51$ (f) smooth s., very fine particles, $\alpha_s = 0.55$

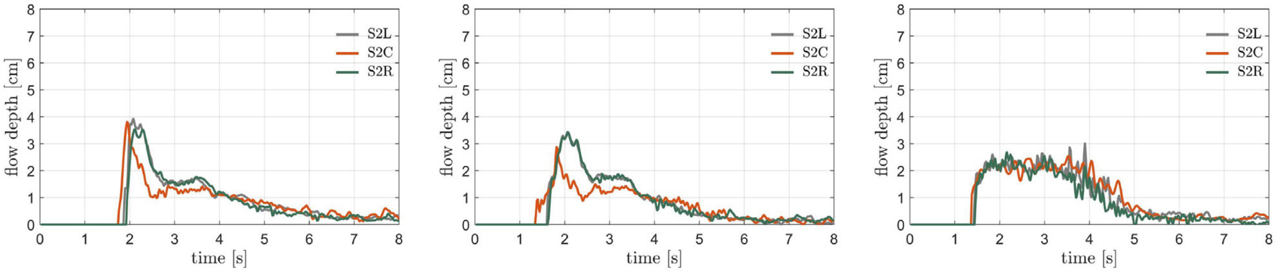

(g) smooth s., very fine particles, $\alpha_s = 0.47$ (h) smooth s., fine particles, $\alpha_s = 0.47$ (i) smooth s., coarse particles, $\alpha_s = 0.47$

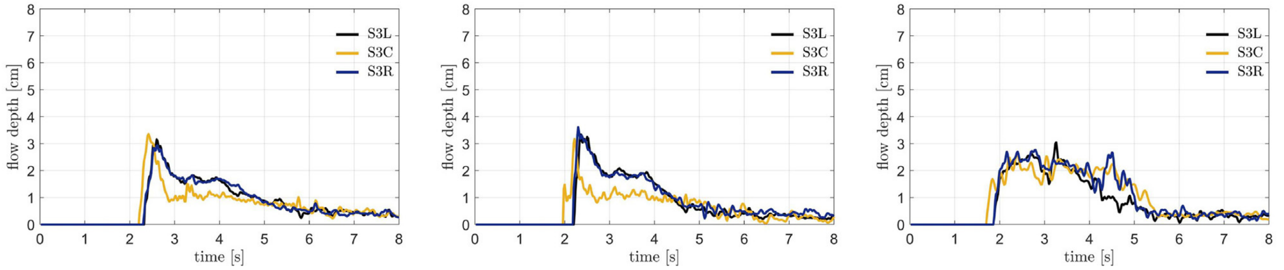

(j) smooth s., very fine particles, $\alpha_s = 0.47$ (k) smooth s., fine particles, $\alpha_s = 0.47$ (l) smooth s., coarse particles, $\alpha_s = 0.47$

Fig. 4. Selection of the flow depth measurements in the **second and third cross-section** for the experiments over **smooth surface** and the same subsets as in Fig. 3 first and second row. Subsets that showed rather unsteady condition (smooth surface, α_s=0.43) are shown in Appendix B.

fraction was (Fig. 3b, c). The debris front is followed by a thin debris body (Fig. 3a, b). The hydrographs for fine particles have also a mature front (Fig. 3e), but which is not developed as a prominent spike like for very fine particles. No sharp debris front peak was observed for coarse particles, even if the solid volume fraction was very low. The overall flow depth pattern for the coarse particles is characterised by an elongated and rounded debris body similar in shape for all solid volume fractions (Fig. 3f and Figures of coarse particles in the Supplementary).

4.1.1.2. Equal solid volume fraction and varying particle size. Evaluating the effect of change of the particle size, we came across that in general larger particles ran faster than smaller ones under the same solid volume fraction (Fig. 3 second row). For every solid volume fraction, the fine particles reached the first sensor S1C 0.2 s earlier than very fine particles. Coarse particles were even 0.1 s faster than fine particles. Flows with very fine particles achieved only equal triggering times of sensor S4C compared to fine and coarse particles under noticeable higher water content. The time delay by smaller particles, in reaching the sensors, as compared to the larger particles, is connected with the amplification of the frontal surge. Small particles result in an amplified frontal surge especially in connection with high water content, but, the flow velocity was a bit lower compared to larger particles. Because the total grain to grain friction was lower for larger particles, coarse particles could not produce any dominant peaks on a smooth surface but could flow faster compared to smaller grains with the same solid volume fraction.

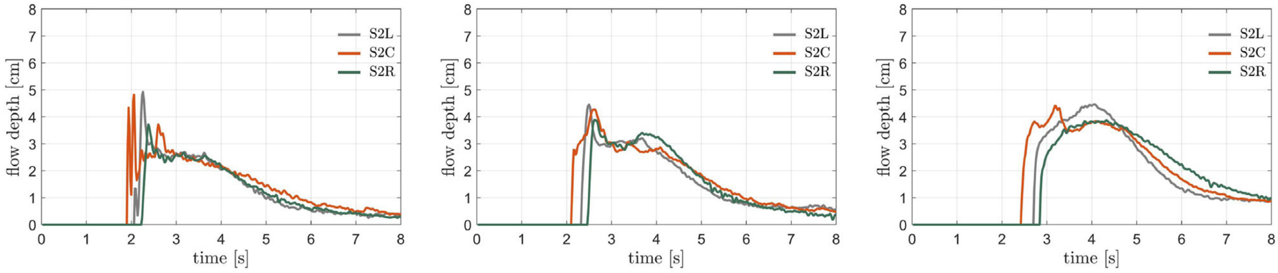

(a) rough s., fine particles, $\alpha_s = 0.43$ (b) rough s., fine particles, $\alpha_s = 0.47$ (c) rough s., fine particles, $\alpha_s = 0.51$

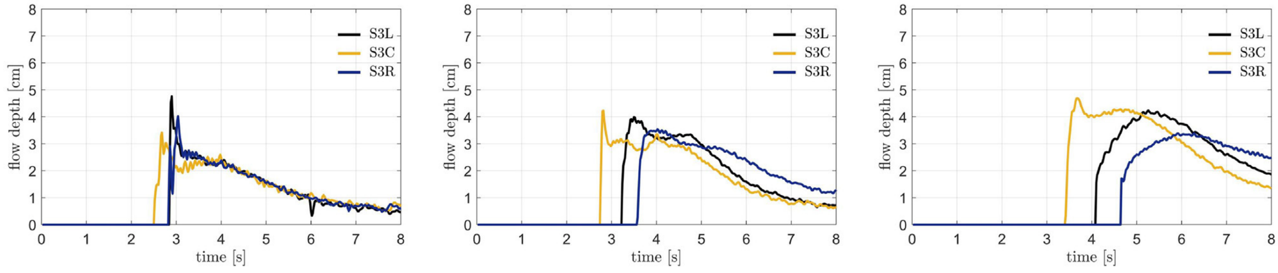

(d) rough s., fine particles, $\alpha_s = 0.43$ (e) rough s., fine particles, $\alpha_s = 0.47$ (f) rough s., fine particles, $\alpha_s = 0.51$

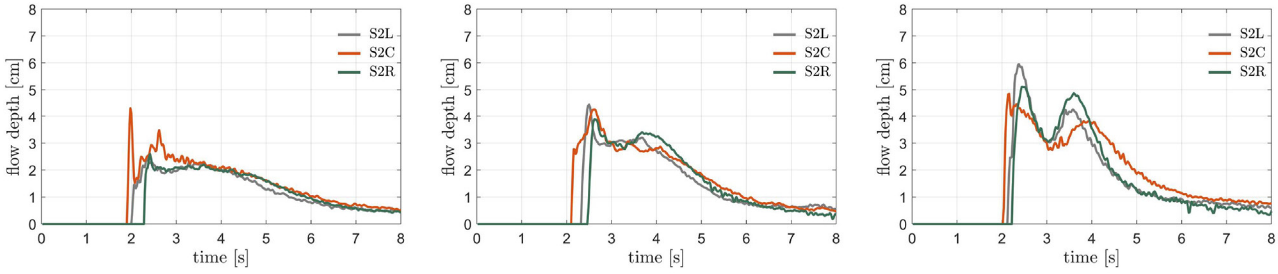

(g) rough s., very fine particles, $\alpha_s = 0.47$ (h) rough s., fine particles, $\alpha_s = 0.47$ (i) rough s., coarse particles, $\alpha_s = 0.47$

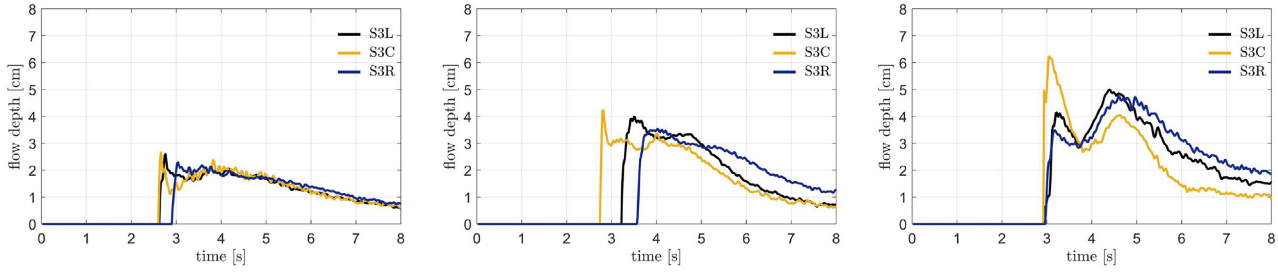

(j) rough s., very fine particles, $\alpha_s = 0.47$ (k) rough s., fine particles, $\alpha_s = 0.47$ (l) rough s., coarse particles, $\alpha_s = 0.47$

Fig. 5. Selection of the flow depth measurements in the **second and third cross-section** for the experiments over **rough surface** and the same subsets as in Fig. 3 third and fourth row.

4.1.1.3. Lateral flow development. Evaluating the flow on the smooth basal surface (Fig. 4), the graphs confirm the general flow characteristics already observed in Fig. 3 (very fine particles: steep frontal surges, fine particles: steep but lower peaks, coarse particles: rounded profile). Comparing the flow depth in lateral directions also highlights that, by tendency, the debris front reached the centre position first in all cases. In most subsets, the lateral devices were reached immediately after the centre devices. Despite this short time delay, the debris front heights were generally comparable between lateral and centre positions. Thus, front shapes were not straight but horizontally levelled over the flume width. Recorded videos confirmed that the debris front usually created a round-shaped dam of similar height along the second and third cross-section (compare e.g. video CS-SS-FP-ALPHA051). But, we had also observed that the debris body formed a different traverse profile. Especially in the third cross-section (S3L, S3C, S3R) a larger amount of sediment had accumulated at the flume sides sliding downwards with lower speed revealing phase-separation. The hydrographs for the left and the right sensors for α_s=0.51 reflect that these sensors were triggered a few milliseconds after the corresponding sensor in the centre (Fig. 4c, f). The discrepancy to this trend occurred when we conducted experiments with smaller particles, in particular under low solid volume fractions (Fig. 4 third and fourth row). Although the debris front was cone-shaped right after the release in these cases, the debris front eventually reached all sensors along the second and third cross-section nearly simultaneously. We found out that this happened when a second more watered debris mass rush disembarked the reservoir and overtopped the slower moving first surge along the whole flume width.

4.1.2. Rough surface

It is to be expected that higher basal friction decreases the sediment travel speed when all other parameters remain unchanged. In general, the rough surface slowed down the velocity in our experiments and, thus, the debris front needed more time to reach the same point as under smooth basal conditions. Although sensor S1C again sensed the debris front about 1 s after the debris release in all rough subsets (Fig. 3 third and fourth row), the additional times needed to reach all succeeding sensors were substantially longer than for a smooth surface. The rough bottom enhanced the bottom shear stress, which slowed down the movement and thus, the debris front was more thwarted than under a smooth condition. However, the following sediment pushed the slower front from behind and contributed to steepen the frontal surge, which was observable in all rough subsets. Thus, the front heights were noticeably higher than on the smooth surface and usually formed a positive step-like bore (Kattel et al., 2016, 2018), which typically occur in natural flows over rough basal surfaces (Takahashi, 1983). We detected nearly double time gaps between signal occurrences at sensor locations in every rough subset compared to smooth bed conditions. Only an increase in the water content had the same acceleration effect as for a smooth bed. The lower the solid volume fraction was, the earlier the debris front reached a specific sensor location.

4.1.2.1. Equal particle size and varying solid volume fraction. Comparing the results for equal particle size (Fig. 3 third row) revealed again that solid volume fraction plays a major role in flow dynamics. The hydrograph for the fine particles shows rapid flows with steep frontal surges, which was detected in all sensor positions. The recorded frontal peaks become again equalized and the flow slowed down when the solid volume fraction was increased (Fig. 3i). For α_s=0.51 the majority of the sediment even remained in the flume after the debris motion has ground to a halt. The same effect has been observed for the very fine particles. A reduction of the water content reduced the flow velocity in these subsets, too. The front peaks were also present but by tendency higher when the solid volume fraction was increased. Coarse particles show similar hydrographs for α_s=0.43 and α_s=0.47, but flow behaviour changed for the highest solid volume fraction α_s=0.51 (figures for coarse particles in the Supplementary). For this subset, the flow velocity was comparatively slow. Sensor S1C registered a steep frontal surge, followed by a small plateau and during the further flow followed by a second huge rounded surge. But flow behaviour changed during routing. Sensor S2C was equally triggered by this flow characteristic but the sediment had formed a rather dense mass when arriving at the third sensor location. Although sensor S4C was still triggered by the debris front, the flow had almost come to a rest.

4.1.2.2. Equal solid volume fraction and varying particle size. Flows over the rough surface with solid volume fractions of α_s=0.47 are characterised by a rapid flow behaviour with a steep frontal surge registered in every cross-section (Fig. 3 fourth row). The moments, when the sensors were triggered were similar for the different particle sizes. While larger particles had flown the fastest on a smooth surface, they were noticeably slower compared to small particles for the rough basal condition. For very fine particles, a prominent flow depth spike is accompanied by a long-drawn-out debris body, which declined in height (Fig. 3j). But barely visible for very fine and fine particles, the hydrograph for the coarse particles show an inherent second surge in the debris body (Fig. 3l). Quite equal in magnitude compared to the debris frontal surge, this more rounded enhancement of the flow depth is noticeable revealed when passing the third and fourth sensor. The reason for that was, that a rather dense sediment disembarked the reservoir first and developed with a steep front but was later cannibalized by the following main sediment amount.

4.1.2.3. Lateral flow development. In general, the hydrographs, which were recorded by the lateral sensors (Fig. 5), show similar trends as the sensors in the centre (Fig. 3 third and fourth row). However, the figures for very fine particles highlight the rapid reduction of the massive front peak, when the sediment flowed from the second to the third cross-section (Fig. 5g, j). Furthermore, the results for the rough surface reveal, that the left sensors (S2L, S3L) were triggered noticeable earlier than the right sensors (S2R, S3R), which is especially eye-catching for fine particles for $\alpha_s \geq 0.47$ (Fig. 5 first and second row) and very fine particles. Thus, the flow is slightly shifted to the right. This effect did not occur for the smooth basal roughness, because flow velocity was probably too high to recognize a significant time delay. However, even if the video records confirm that effect (compare e.g. video CS-RS-FP-ALPHA047), an obvious reason for that remained uncertain.

4.2. Evaluation of the debris mass

We evaluate the data from the load cells to gain complementary information about the flow dynamics. As already mentioned in Section 2.2, the load cells exhibited slightly inert behaviour during data acquisition. The rapid flow over the smooth surface caused a non-synchronous acquisition of mass data and the associated time signal. Unfortunately, the generated mass hydrographs were not meaningful. However, the time delay was negligible for flows over the rough bed. Thus, we present only these results in the following with the hydrographs along the centre line in Fig. 6 and for the lateral sensor positions in Figs. 7 and 8.

4.2.1. Equal particle size and varying solid volume fraction

The results for the very fine particles (Fig. 6 first row) and fine particles (Fig. 6 second row) show relatively similar results. Sensor S1C always registered a sharp and dominant peak, which, in general, is slightly reduced with increasing solid volume fraction. In contrast, the mass of the debris front over sensor S2C was very low but increased again when triggering sensor S3C and S4C. Only for fine particles and α_s=0.47, the mass over S4C was lower than over S3C (Fig. 6e). The reason for the diminished mass over S2C is due to phase-separation. The experiments started with a relatively compact and viscous sediment mixture. However, particles could concentrate at the bottom of the reservoir box and disembark the reservoir preferentially and hence trigger sensor S1C first. But, higher dilute material was leaving the sediment box afterwards and usually overtopped the first surge between S1C and S2C. Due to higher water content, the now mixed up flow exhibited lower mass, which is seen in the reduced mass of S2C. On the way to the third measurement section, the remixed material began to separate again into a grained front and a diluted debris body, a phenomenon often observed in debris flow (de Haas et al., 2015; Pudasaini and Fischer, 2020b). Thus, sensor S3C registered again a high-mass front surge, which usually became even enhanced at sensor S4C. Depending on the solid volume fraction, a second diluted surge followed the debris front and overtopped the already separated flow between the third and the fourth measurements cross-section. Therefore, the remixing process could happen a second time in conjunction with a diminished surge height (Fig. 6e). The mass-evolution of coarse particles were characterised by two dominant surges, often equal in height (Fig. 6g–i). The first surge usually represents the initial particle dominated debris front followed by a small amount of diluted debris body. This clearly shows the particle-fluid phase separation: particle dominated front and viscous fluid dominated back (Pudasaini and Fischer, 2020b). The second surge was assembled by the remaining sediment in the reservoir and followed the diluted debris body almost equal in length and height as the first surge. Especially for α_s=0.43 and α_s=0.47, the peak heights of the surges are comparable. A lower and V-shaped part of the hydrograph lays in-between

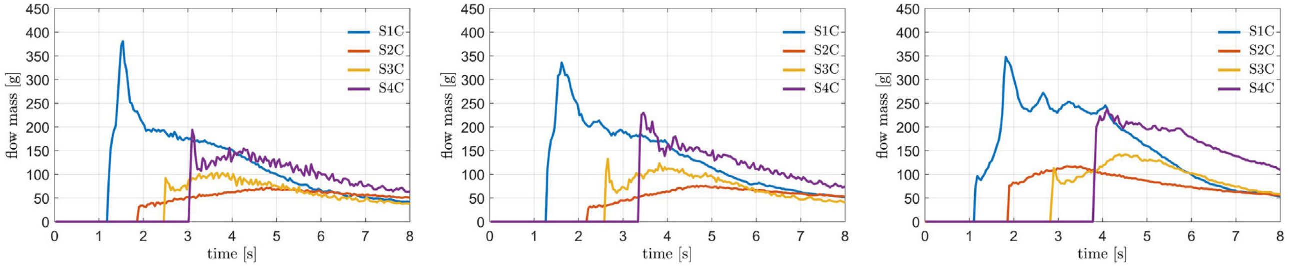

(a) rough s., very fine particles, $\alpha_s = 0.43$ (b) rough s., very fine particles, $\alpha_s = 0.47$ (c) rough s., very fine particles, $\alpha_s = 0.51$

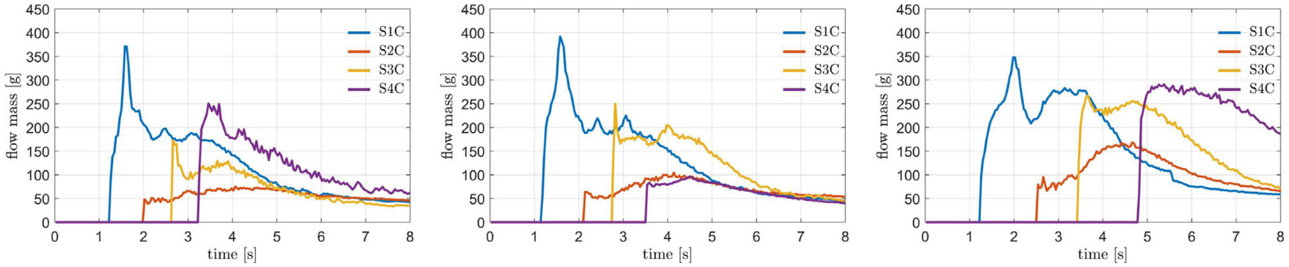

(d) rough s., fine particles, $\alpha_s = 0.43$ (e) rough s., fine particles, $\alpha_s = 0.47$ (f) rough s., fine particles, $\alpha_s = 0.51$

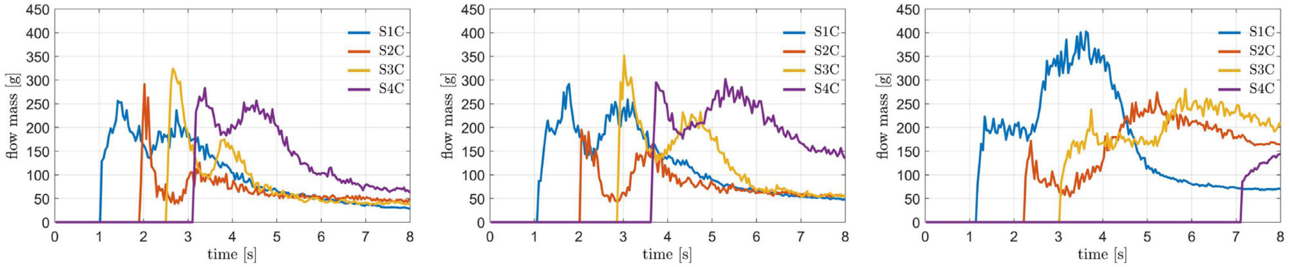

(g) rough s., coarse particles, $\alpha_s = 0.43$ (h) rough s., coarse particles, $\alpha_s = 0.47$ (i) rough s., coarse particles, $\alpha_s = 0.51$

Fig. 6. Measured mass data for the experiments with very fine, fine and coarse particles in three different initial solid volume fractions. The four measurement stations are located along the flume centre line in the downslope direction.

these peaks, that result in an inhomogeneous flow for these subsets with coarse particles.

4.2.2. Equal solid volume fraction and varying particle size

As mentioned before, the mass-evolution for very fine particles (Fig. 6 first row) and fine particles (Fig. 6 second row) show comparable results (exceptions in Fig. 6b and e). Only the enhancement of the particle size to coarse particles let the flow generate two dominant surges. By comparing the left and the middle column in Fig. 6 reveals, that a change in particle size has no observable effect on the front velocity. In contrast, the flow slowed down with increasing particle size for α_s=0.51 (Fig. 6 right column).

4.2.3. Lateral flow development

Figs. 7 and 8 show the results in measurement cross-section 2 and 3 and therefore provide information about the lateral mass profiles. The graphs in cross-section 2 for very fine particles and fine particles display the already mentioned low mass values in the centre location (Fig. 7a, b, c, g, h, i). The mass at the debris front was low during this specific point of time because the diluted surge had overtopped the coarse front between the first and the second cross-section. One would expect, that the mass should be low in the lateral measurement spots as well. But, the graphs for the cross-section 2 display the opposite. The mass alongside the lateral locations is high for very fine particles and fine particles independently from solid volume fraction. Flow depth was nearly similar in the lateral direction in cross-section 2. Thus, the bulk debris over the lateral load cells must have higher mixture densities. The diluted surge overtopped the front mainly in the centre of the flume, where the flow velocity is usually higher than close to the lateral boundaries. Simultaneously, the surge shouldered aside the grained and relatively dry debris from the front and displaced it over the lateral sensors, that record higher mass values. Even if the experiments with coarse particles show similar differences in the graphs in cross-section 2 (Fig. 8a, b, c), the effect of phase separation was not in the same way distinctive. This natural phenomenon of phase separation continued in our experiments when the flow front moved towards cross-section 3. The graphs in the third cross-section revealed that the mass in the lateral spots remained at comparable height as recorded in cross-section 2. But, the mass in the corresponding centre location is increased noticeably. On its way towards cross-section 3, the flow began to develop back into a grained front and a diluted debris body following behind. This can be seen in Fig. 7d, e, j, and k where a small steep debris front is already accomplished. A section with lower mass follows directly the front. However, the phase separation process was not finished when the flow front triggered the third cross-section, because the mass is still not equalized along with the lateral profile. For α_s=0.43 and α_s=0.47 the phase separation took also place for the coarse particles (Fig. 8). Two distinctive surges were well developed along with both lateral profiles for each subset. The large grains facilitate compensation of water differences between the phases due to higher pore volume. However, a high solid volume fraction led to an inert flow behaviour with hindered phase separation (Fig. 8 right column).

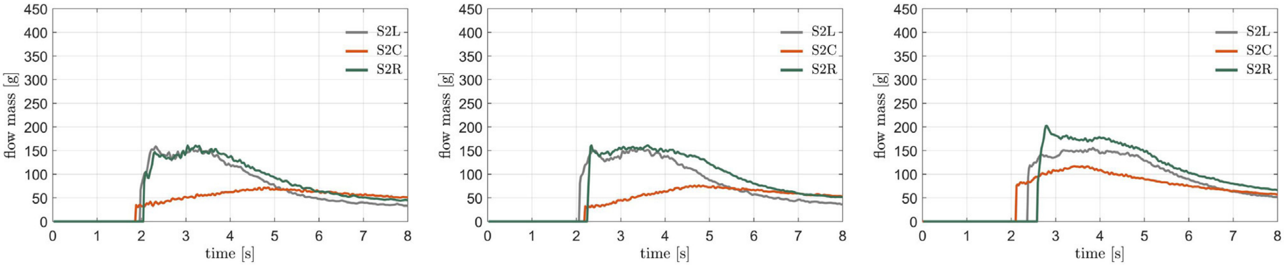

(a) rough s., very fine particles, $\alpha_s = 0.43$ (b) rough s., very fine particles, $\alpha_s = 0.47$ (c) rough s., very fine particles, $\alpha_s = 0.51$

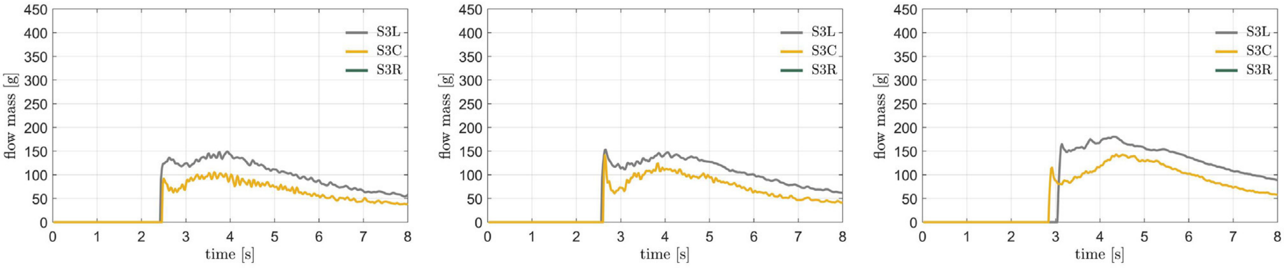

(d) rough s., very fine particles, $\alpha_s = 0.43$ (e) rough s., very fine particles, $\alpha_s = 0.47$ (f) rough s., very fine particles, $\alpha_s = 0.51$

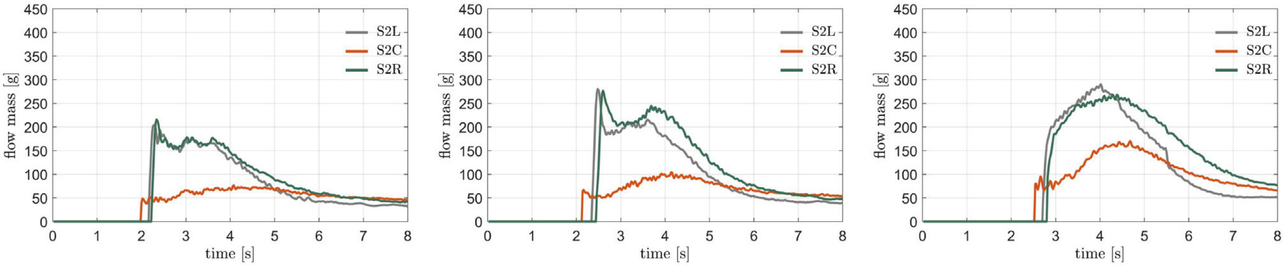

(g) rough s., fine particles, $\alpha_s = 0.43$ (h) rough s., fine particles, $\alpha_s = 0.47$ (i) rough s., fine particles, $\alpha_s = 0.51$

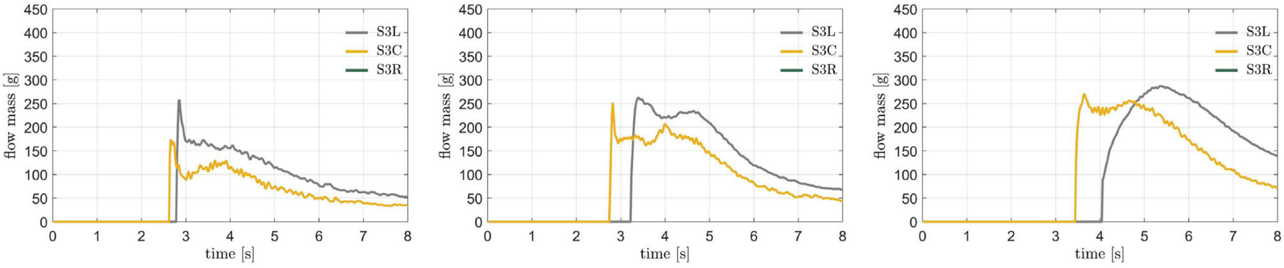

(j) rough s., fine particles, $\alpha_s = 0.43$ (k) rough s., fine particles, $\alpha_s = 0.47$ (l) rough s., fine particles, $\alpha_s = 0.51$

Fig. 7. Juxtaposed mass measurements in the second and third cross-section for the experiments with very fine and fine particles for α_s=0.43, α_s=0.47 and α_s=0.51 on a rough bed. Unfortunately, sensor S3R had been malfunctioned and could not provide data properly.

4.3. Depth-averaged bulk density

As one of the key dynamical variables in mixture mass flow models (Pudasaini, 2012), the local depth-averaged bulk density is an estimation of the evolution of solid volume fraction and provides the flow depth. Combining data from the ultrasonic transducers and the load cells enabled us to calculate the local depth-averaged bulk density in rough-surface subsets

$$\rho_{bulk} = \frac{p}{gh\cos\theta} = \frac{m}{A_{PVC}h\cos\theta} \tag{3}$$

during sediment motion (Fig. 9). For recalculation, one need the measured data of the debris mass m, the flow depth component perpendicular to the flume plane $h\cos\theta$ (both data found in the Supplementary), and the circular area of the PVC-plates A_{PVC} (with 7 mm diameter, compare Section 2.2). The calculation of the depth-averaged bulk density in Eq. (3) reacts sensitive to very high or very low values of mass and flow depth. Both were partly registered by the sensors in the experiments when the debris front triggered the sensors initially, especially in the first (S1C) as well as in the second measurement cross-section (S2C, S2L, S2R). Sensor S1C was highly influenced by the first surge of the headgate opening, resulting in heavy fluctuating densities at the debris front (Fig. 9c, i). The calculation of the bulk density in the second cross-

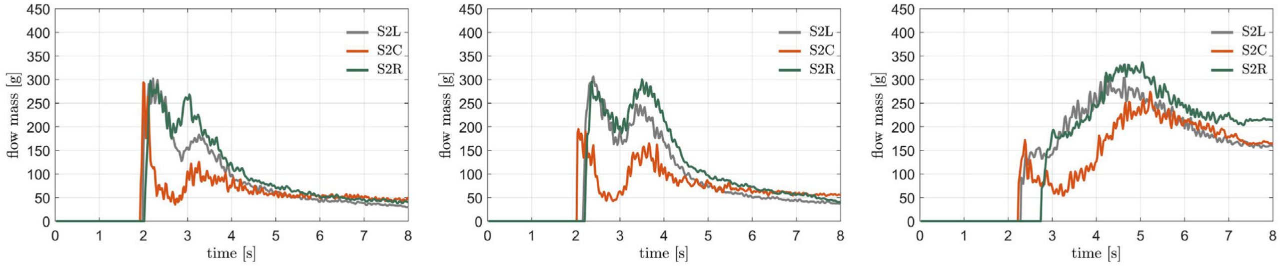

(a) rough s., coarse particles, $\alpha_s = 0.43$ (b) rough s., coarse particles, $\alpha_s = 0.47$ (c) rough s., coarse particles, $\alpha_s = 0.51$

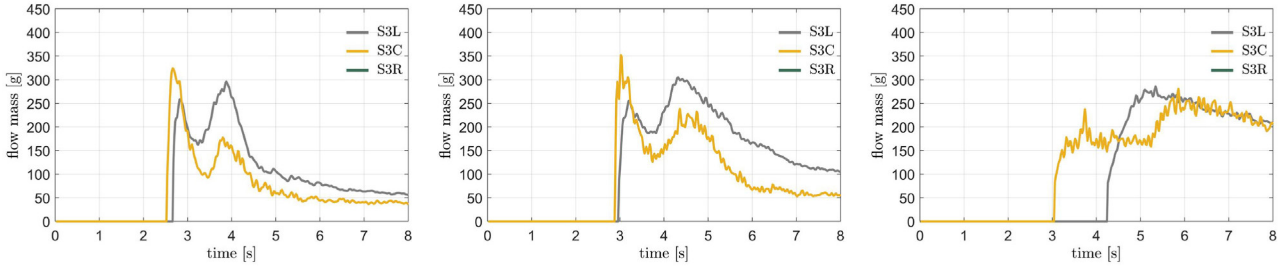

(d) rough s., coarse particles, $\alpha_s = 0.43$ (e) rough s., coarse particles, $\alpha_s = 0.47$ (f) rough s., coarse particles, $\alpha_s = 0.51$

Fig. 8. Juxtaposed mass measurements in the second and third cross-section for the experiments with coarse particles for α_s=0.43, α_s=0.47 and α_s=0.51 on a rough bed. Unfortunately, sensor S3R had been malfunctioned and could not provide data properly.

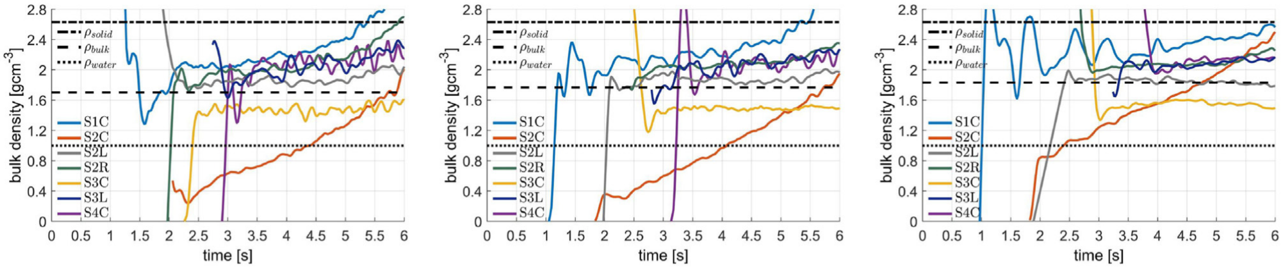

(a) rough s., very fine particles, $\alpha_s = 0.43$ (b) rough s., very fine particles, $\alpha_s = 0.47$ (c) rough s., very fine particles, $\alpha_s = 0.51$

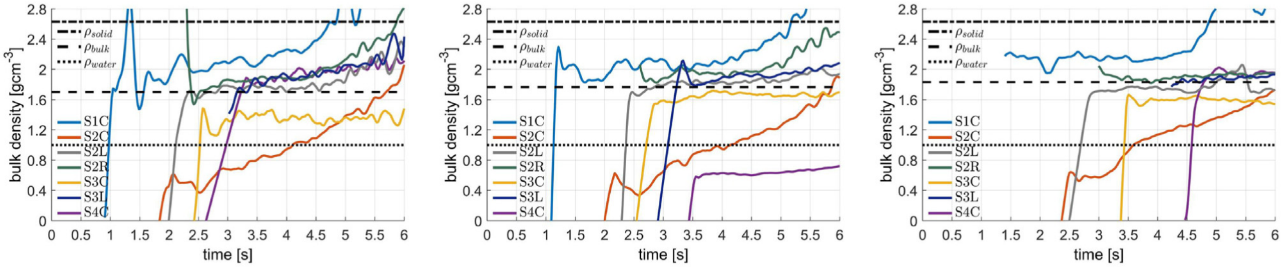

(d) rough s., fine particles, $\alpha_s = 0.43$ (e) rough s., fine particles, $\alpha_s = 0.47$ (f) rough s., fine particles, $\alpha_s = 0.51$

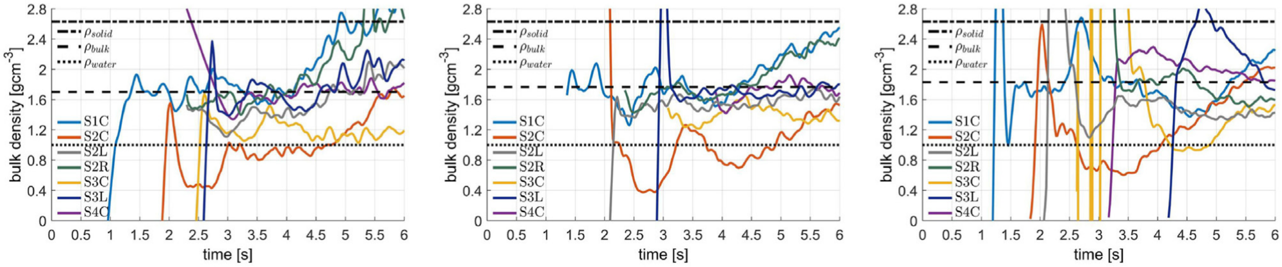

(g) rough s., coarse particles, $\alpha_s = 0.43$ (h) rough s., coarse particles, $\alpha_s = 0.47$ (i) rough s., coarse particles, $\alpha_s = 0.51$

Fig. 9. The local depth-averaged bulk density evolution at the sensor positions (sensor S3R excluded) determined from flow depths and load cell data for subsets with the rough basal surface. For comparison, the density of the solid particles, the density of water and the bulk density of the initial mixture in the reservoir is plotted as lines.

section suffered from the second surge of the particle-fluid mixture, which overtopped the first flush in the centre of the flume in the range of sensor S2C. This turbulent phenomenon results in high depth values, which was not represented equally by a corresponding mass registered by the load cells and lead to doubtful low density value at sensor S2C in all experiments. After the main debris passed a sensor, accumulations of single grains remained at the measurement locations, which triggered the ultrasonic sensors, though, but the mass was too low to achieve a clear signal for the load cells. Because of that, the bulk density raises unusable higher as the density of the solid particles. Therefore, one can ignore density data which is calculated approximately 5 s after a sensor is initially triggered.

In Fig. 9, we additionally plotted the lines of the density of the solid particles, the density of water and the bulk density of the initial mixture in the reservoir. The bulk density is meaningful only if it lies between the true particle and fluid density in the mixture. Because the particles in the mixture settled in the reservoir after dumping and mixing, this more granular part exiting the headgate area first and reached sensor S1C before the more watered remnant overtopped it over S2C. This is seen in Fig. 9, where the bulk density at S1C is usually equal or over the initial bulk density. Thus, the solid volume fraction must be higher than the initial prepared value. The front overtopping at the second measurement cross-section results in very low bulk densities at S2C. Nevertheless, the remixed sediment should show solid volume fraction similar to the initially prepared mixture. The comparison of sensor S2C with the corresponding lateral sensors S2L and S2R reveal, that the overtopping occurred mainly in the flume centre and that the lateral bulk densities are comparable with the values in the reservoir. Overall, the moving mixture can be assumed as almost in steady and uniform motion when arriving the third sensor cross-section. We have to mention, that due to the malfunction of the load cell S3R, the density could also not be calculated at that position. However, all subsets in Fig. 9 show, that the bulk density at the centre (S3C) is between the density of water and the initial prepared density in the reservoir. The lateral sensor (S3L) shows comparable values as that in the reservoir. Thus, as we discussed above, particles were shouldered aside during motion and a watered mixture concentrated in the centre of the flume. This is a typical situation in phase separation in mixture mass flows (de Haas et al., 2015; Pudasaini and Fischer, 2020b) Here, the mixture exhibits lower and at the lateral positions a higher solid volume fraction than in the reservoir. There is no clear difference in the density profiles for different particles sizes. For some subsets, one can notice a head-body diversion of the flow in the third cross-section (Fig. 9b, c, d, f, g, h) with an approximately 0.2 s long more granular debris front with bulk densities around $1.6\,\mathrm{g\,cm^{-3}}$ and a more dilute body with bulk densities around $1.2\,\mathrm{g\,cm^{-3}}$ equally in length. The bulk density at the debris front had been enhanced significantly owing to grain accumulation while the debris body behind the front had lower density values as in hyperconcentrated flows (Costa and Williams, 1984). This resulted in a separation between particle and fluid (de Haas et al., 2015; Pudasaini and Fischer, 2020b). After the dilute body, the bulk density of the tail raised again to roughly $1.5-1.6\,\mathrm{g\,cm^{-3}}$. In other subsets, the bulk density proceed rather equally (Fig. 9a, e). Fig. 9i shows too high fluctuation of bulk density at S3C. The density in the fourth cross-section (S4C) shows, in general, high values than at S3C. The front had accumulated more granular part of the flow and, therefore, exhibited a density comparable to the initial value in the reservoir. The debris front for fine particles and α_s=0.47 (Fig. 9e) had a very long and narrow snout, because the very dilute sediment was concentrated in the centre of the flow. The flow depth was therefore high there, but the mass was relatively low which lead to such exceptional low bulk density over S4C for this subset.

Overall, the evaluation of the density evolution reveals, that the density, and therefore the solid volume fraction of the particle-fluid mixture, changed during the flow (from initiation until deposition). Although the initial density of the debris mixture appears to be rather similar (1701 kg $\mathrm{m^{-3}}$ and 1902 kg $\mathrm{m^{-3}}$) we see significant differences in the calculated bulk density varying between the density of water and the density of the particles. This is consistent with reality. Together with the evolution of the flow depth and the mass, the density profiles indicate that the mixture needed half the flume length to develop into a steady and uniform moving debris mass and was shaped due to phase separation effects. However, the local value of the bulk density was also influenced by the mixture velocity and the shape of the debris front.

Since ρ_{solid} and ρ_{water} are known from the material parameters of the solid and fluid (densities) and ρ_{bulk} is obtained from the measurements, from the equation of the bulk density (1), we obtain the solid volume fraction evolution

$$\alpha_s=\frac{\rho_{bulk}-\rho_{water}}{\rho_{solid}-\rho_{water}}=\frac{\chi_w^b-1}{\chi_w^s-1} \tag{4}$$

where $\chi_w^b=\rho_{bulk}/\rho_{water}$, and $\chi_w^s=\rho_{solid}/\rho_{water}$ are the bulk to fluid, and solid to fluid density ratios. Because $\chi_w^s>\chi_w^b$; $\alpha_s\in(0,1)$. With the knowledge of the dynamically evolving α_s from experiments, importantly α_s can be used to validate the two- or multi-phase mass flow models (Pudasaini and Mergili, 2019) because α_s is a dynamical state variable in the mixture mass flow models.

4.4. Evaluation of debris front velocity and shape

We recorded video camera data to explore the debris front velocity and shape, which both are thumb-print indicators for debris flow dynamics. The reader can find all videos in the Supplementary source. We tracked the position of each flow front beginning right after the release until the debris reached the runout plane. In post-processing, the image analysis allowed us to determine the temporal evolution of the debris front velocity and shape during the runs (Figs. 10 and 11). We evaluated the data when the first part of the debris front overran each of the four measurement cross-sections and when the front entered the runout plane.

4.4.1. Front velocity

Fig. 10 illustrates the debris front positions over time as well as the front velocity, both for a smooth and rough surface. The abscissa depicts the time, which was synchronized with the flap opening. The ordinate in the upper rows of the subplots depicts the position of the debris front with the zero value at the reservoir outflow. The other five positions are the four measurement cross-sections and the entry to the runout plane. The front position graphs gave us an approximation about the mean debris front velocity between two data points of the front position. This is shown in the lower rows. All plotted front positions are superimposed for the first seconds showing a constant flow speed. But, almost every subplot illustrates a subsequent sharp bend at a specific time, except for the coarse particle over the smooth surface, which shows a distinct behaviour. One could think that this was due to the sudden flow acceleration. But cross-checking data with video records revealed that this sudden flow velocity enhancement was always provoked by a highly dilute second trailing surge (compare e.g. video CS-RS-VP-ALPHA043). It departed rapidly from the reservoir and overtopped the slower initial surge 1 to 2 s after flap opening. This resulted in an abrupt enhancement of the front velocity. On a smooth surface, this overtopping occurred earlier the smaller the particles were. For the coarse particles, we had not observed any substantial overtopping in smooth basal subsets (Fig. 10c) since the second surge was not so dominant and could not reach the first surge before it entered the runout plane. Under the rough basal condition, overtopping occurred earlier compared to the smooth surface. Here, the first surge faced higher basal friction and was not able to gain comparable speed as for the flow with smooth surface conditions. Therefore, the first surge had covered less distance when the second surge

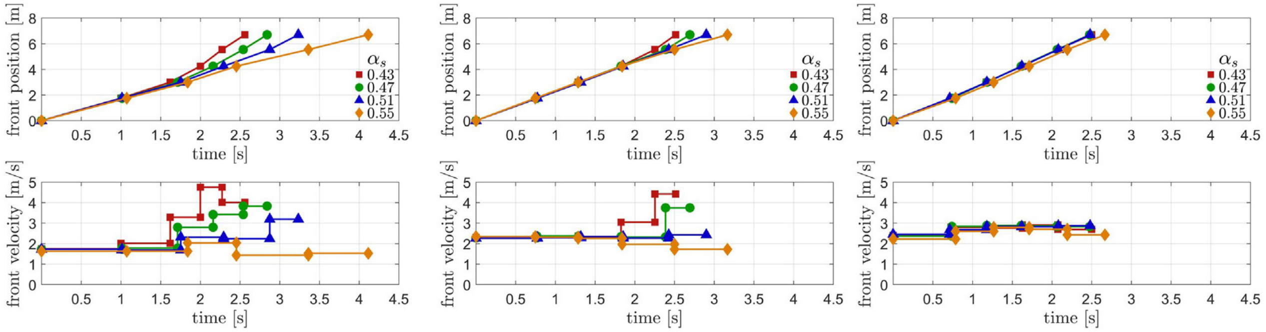

(a) smooth surface, very fine particles (b) smooth surface, fine particles (c) smooth surface, coarse particles

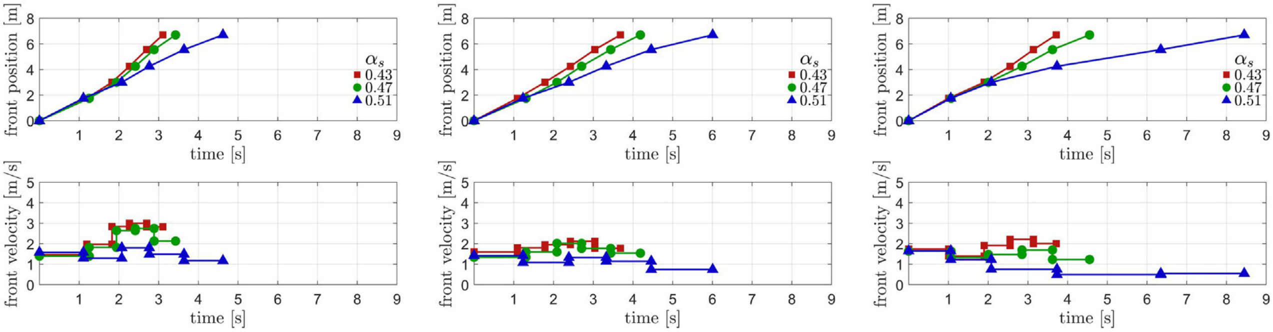

(d) rough surface, very fine particles (e) rough surface, fine particles (f) rough surface, coarse particles

Fig. 10. Debris flow front position over time for different solid volume fractions and particle sizes over smooth and rough basal surface.

overtopped it. In most cases, the cumulated surges flowed with enhanced steady-state velocities after surge-merging, which are shown by higher gradients and enhanced velocities in the corresponding panels. However, a more nonlinear enhancement of the front position over time was present in subsets with very fine particles (Fig. 10a). As a result, mostly the front velocity raises more and more during the run. A lower solid volume fraction resulted in higher front velocities after surge-merging, though, the cumulated surge was also decelerating with high solid volume fractions. This is shown by a front position over time with a lower gradient and decreasing front velocities (Fig. 10d–f). For each of these deceleration subsets, we cross-checked the video records for the rough surface and identified steep gravel-rich flow fronts rolling over the rough bed. This reveals typical particle-fluid separation in a debris flow. In combination with the high basal friction, the relatively large normal force at the front diminished the velocity of the flow.

4.4.2. Front shape

The basal roughness and the particle size played a shape-determining role in all experiments (Fig. 11). We clearly observed that higher basal friction, as well as coarse, and fine particles promote rounded, nearly parabolic, front shape with the tip along the centre line. The parabolic front was dominant until the mixture had flown half the way down the flume (Fig. 11b, c, e, f). The trailing and more dilute debris body had transversely a rather straight shape. Henceforth, this portion of the debris body moved faster than the centre front. That is why the lateral sediment was accelerated faster and eventually moved at the speed of the central front. As a result, the front shape became transversally straighter during motion (Fig. 11b, c). All subsets with coarse and fine particles showed a rather dense flow behaviour, that is why the front shape and overall dynamics was comparable for different solid volume fractions (Fig. 11b, c, e, f). The experiments with very fine particles showed different characteristics (Fig. 11a, d). In these cases, and in particular for a low solid volume fraction, the front geometry had a very rounded shape at the beginning of the run but later moved more chaotically between convex and concave forms or, even unpredictable on the rough surface. The debris front shapes were less predictable because of enhanced lateral waves which bounced back from solid walls and influenced the flowing material in the flume immediately. On the contrary, for high solid volume fractions, the front geometry remains in a rounded shape during the run with very fine particles. Overall, the front shape was mainly influenced by basal roughness and particle size but was less sensitive due to a change in solid volume fraction.

5. Dimensional analysis

In this section, we present the calculated dimensionless numbers for our experiments and compare them with the results from other experimental studies and natural events, but focus especially on the comparison with typical values for natural coarse-grain debris flows as presented in Lanzoni et al. (2017). The dimensionless numbers are calculated according to Table 2 and by using the measured data of flow depth, mass, bulk density, and velocity, as well as the sediment properties (Table 1). A deeper description of the dimensionless numbers is available in Appendix C. All dimensionless numbers are calculated for the debris front when it reached sensor S4C and the flow was in quasi-steady or steady condition. We present the range of our data in Table 3. The dimensionless numbers, which are relevant the most to identify characteristic flow regimes are displayed in Fig. 12. Common lines, which separate flow regimes are plotted additionally. The data in Fig. 12 is already grouped into observed flow types, that is described in detail in Section 6.

We determined **pressure numbers** between $1.1 \cdot 10^4 < N_p < 1.0 \cdot 10^6$. In contrast to a natural flow, where usually small and/or muddy-viscous particles take up fully or partly the pore volume space between larger particles, the debris mixture in our experiments is based on a steep grain size distribution. Thus, the porosity and the hydraulic diffusivity are high and pore water may diffuse and leave the sediment quickly in relation to the flow velocity during motion.

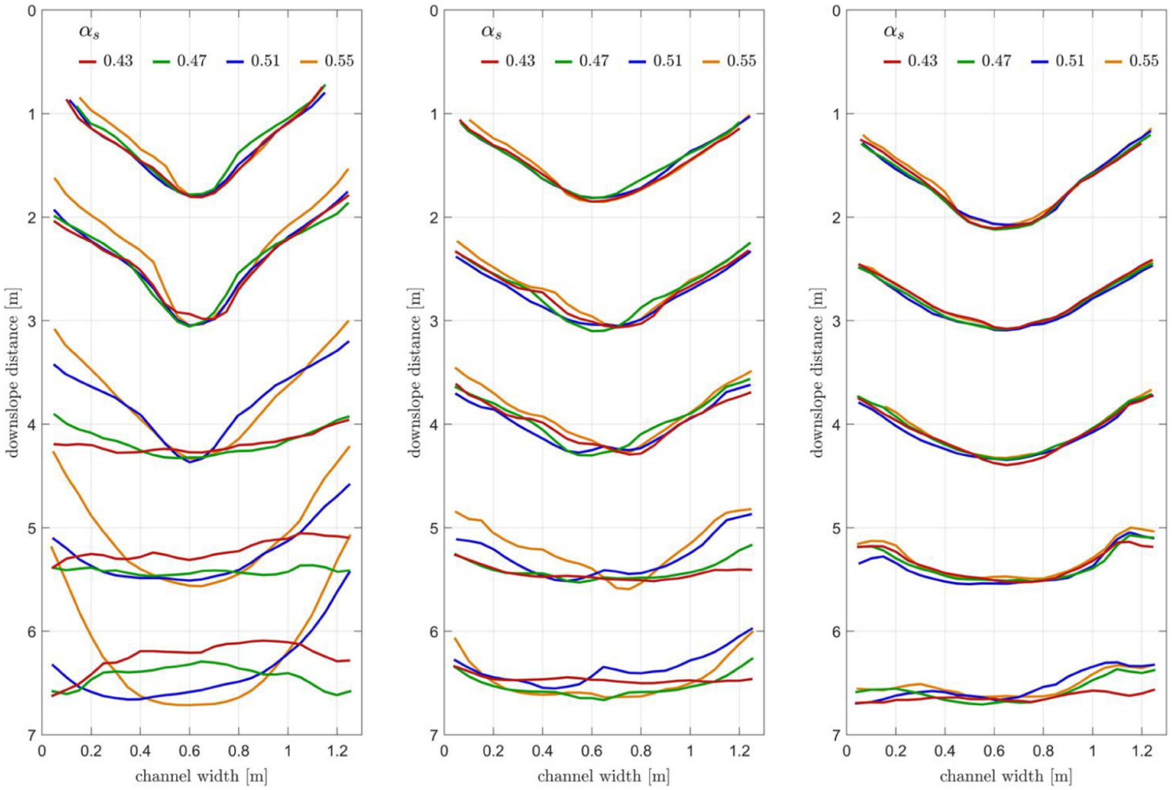

(a) smooth s., very fine particles (b) smooth s., fine particles (c) smooth s., coarse particles

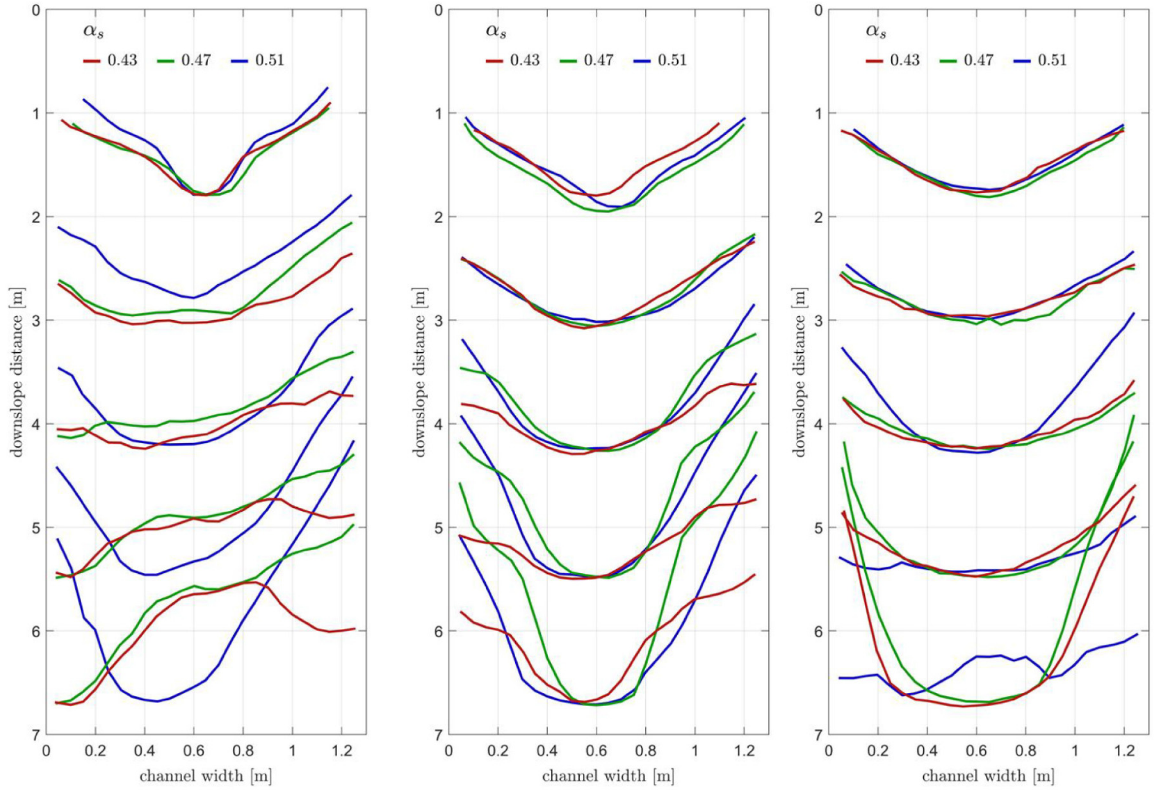

(d) rough s., very fine particles (e) rough s., fine particles (f) rough s., coarse particles

Fig. 11. Evolution of debris flow front shape: Dependencies on basal roughness, solid volume fraction and particle size.

Table 3
Flow variables and dimensionless numbers of this study in comparison with small-scale as well as large-scale experimental debris flows and natural events. The parameters of this study were calculated from the values of the debris front at sensor S4C.

Parameter	Symbol [unit]	Flume experiment (this study)	Flume experiments[b,c,d,e,h]	Natural coarse-grained flows[l]	Typical range natural debris flows[b]
Flow variables					
Grain diameter	$d\,[\mathrm{m}]$	0.00144–0.00625	0.0005–0.002	0.05–0.4	10^{-5}–10
Flow depth	$h\,[\mathrm{m}]$	0.014–0.051	0.005–0.1	0.3–4.3	0.1–10
Flow velocity	$v\,[\mathrm{m\,s^{-1}}]$	0.548–4.423	0.9–10	0.6–9.4	0.1–20
Flow shear rate	$\dot{\gamma}\ [\mathrm{s^{-1}}]$	16.6–157.3	100–371	0.4–5.9[a]	1–100
Solid density	$\rho_{solid}\,[\mathrm{kg\,m^{-3}}]$	2630–2640	2650–2700	2650	2500–3000
Fluid density	$\rho_{water}\,[\mathrm{kg\,m^{-3}}]$	1000	1000–1533	1050–1250	1000–1200
Solid volume fraction	$\alpha_s\,[1]$	0.43–0.55	0.35–0.5	0.30–0.51	0.4–0.8
Fluid viscosity	$\mu\,[\mathrm{Pa\,s}]$	0.001	0.001–0.0035	0.1	0.001–0.1
Basal friction angle	$\delta\ [^\circ]$	25.1–34.0	40–42	–	25–45
Hydraulic permeability	$k\,[\mathrm{m^2}]$	$6\cdot10^{-11}$–$10^{-9\,a}$	$1.1\cdot10^{-16}$–10^{-11}	$1.2\cdot10^{-7}$–$6\cdot10^{-6}$	10^{-13}–10^{-9}
Hydraulic diffusivity	$D\,[\mathrm{m^2\,s^{-1}}]$	51–845	$5.8\cdot10^{-9}$–$1.2\cdot10^{-1}$	–	10^{-8}–10^{-2}[e]
Dimensionless numbers					
Pressure number	N_{press}	$1.1\cdot10^{4}$–$1.0\cdot10^{6}$	0.003–200	–	10^{-6}–10^{-1}[c,d,f]>
Savage number	N_{Sav}	0.014–6.75	0.17–2.25	0.001–1.96	10^{-7}–10^{0}[b,c,f]
Bagnold number[c,g]	N_{Bag}	560–34,985	400[b]	200–45,900	600–$4\cdot10^{8}$[c]
Bagnold number[b,h]	N_{Bag}	201–13,804	37–1589	–	0.2–4[b]
friction number	N_{fric}	984–21,854	$1.4\cdot10^{2}$–$3\cdot10^{3}$	$1.9\cdot10^{4}$–$5.5\cdot10^{5}$	10^{0}–10^{9}[b,c,f]
mass number	N_{mass}	1.984–3.227	1.2–4.0	0.95–2.51	1–10
Darcy number	N_{Dar}	6–317	$6.0\cdot10^{2}$–$5.9\cdot10^{7}$	0.47–760	10^{4}–10^{8}
Stokes number	N_{St}	13–630	–	11–48	–
Froude number[i]	Fr	1.0–8.4	2.9–7.9	0.2–2.4[a]	0.8–6[j,k]
Reynolds number	Re	$1.4\cdot10^{5}$–$5.0\cdot10^{5}$	$2.3\cdot10^{4}$–$1.4\cdot10^{5}$	10^{2}–$4.13\cdot10^{4}$	10^{5}–10^{7}[c,d]
Particle Reynolds nu.	Re_p	1681–17,884	31–504	38–10,340[a]	0.01–2[b,f]

[a] Calculated by assuming a compressibility of the interstitial fluid $C=2\cdot10^{-9}\,\mathrm{Pa^{-1}}$ and a hydraulic conductivity K according to the particle sizes: very fine particles $K=6\cdot10^{-4}\,\mathrm{m\,s^{-1}}$, fine particles $K=2\cdot10^{-3}\,\mathrm{m\,s^{-1}}$, coarse particles $K=1\cdot10^{-2}\,\mathrm{m\,s^{-1}}$. Shear rate, Froude number and particle Reynolds number were calculated according to $\dot{\gamma}=v/h$, Eqs. (C.9), and (C.11). [b] Iverson (1997). [c] Iverson and Denlinger (2001). [d] Iverson et al. (2010). [e] Major (2000). [f] Zhou and Ng (2010). [g] Bagnold (1954). [h] de Haas et al. (2015). [i] Pudasaini and Domnik (2009). [j] Arai et al. (2013). [k] Turnbull et al. (2015). [l] Lanzoni et al. (2017).

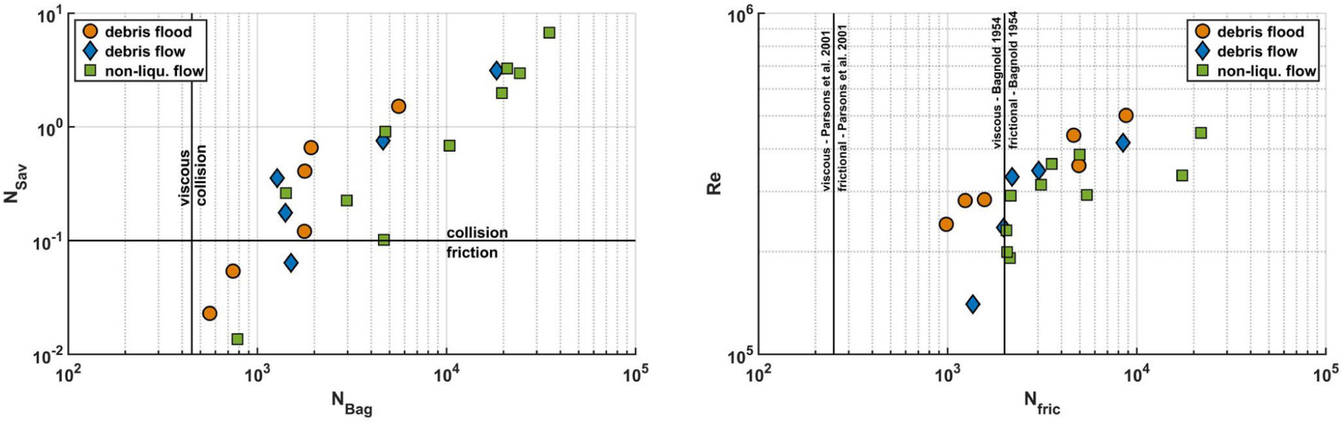

(a) Savage number and Bagnold number

(b) Reynolds number and Friction number

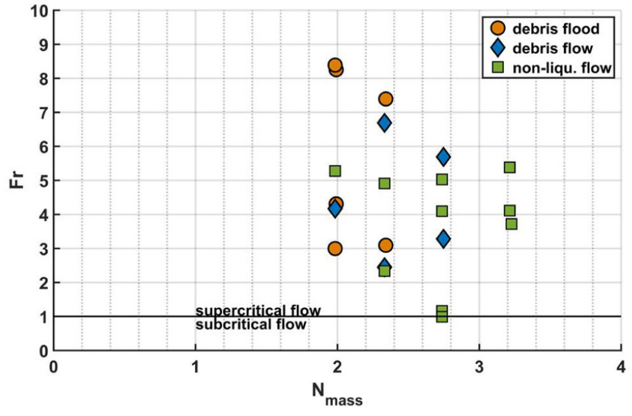

(c) Froude number and Mass number

Fig. 12. Dimensionless numbers of the observed flow types with included common lines, which separate characteristic regimes.

This is reflected in increased pressure numbers for our experimental setup compared to natural events and other experiments (Iverson and Denlinger, 2001; de Haas et al., 2015), which had different material composition. In the presented experiments, pore pressure played a minor role in sediment mobilization in general. Even if high pore pressure values had been developed in the moving mass, decompression developed too quickly to permit a perceptible liquefaction effect.

The range of the **Savage number** was $0.18 \le N_{Sav} \le 6.75$ in the presented experiments for the smooth surface and $0.014 \le N_{Sav} \le 3.13$ for the rough surface (Fig. 12a). Overall, these values are in agreement with natural coarse-grained events (Lanzoni et al., 2017) and other experiments (Iverson, 1997; Iverson and Denlinger, 2001; de Haas et al., 2015). However, flows over the smooth surface were mainly dominated by grain collision stresses because the varnished wooden plates minimised basal friction. The internal friction force was almost negligible compared to grain collision. Furthermore, less water diminished grain to grain distance, which eventually facilitated the collisional force even more. For experiments over the rough surface, the Savage numbers partly fell below 0.1, in particular for high solid volume fractions. Here, the basal water layer could not lubricate sufficiently the gap between bottom near grains and basal roughness, particularly in the flow front. So, the frictional forces had been dominating collisional forces in some rough subsets, that results in the better agreement with documented events (Iverson and Denlinger, 2001).

Using $\alpha_{s,\,max}$=0.7405 (Dullien, 1991), we calculated **Bagnold numbers** between $560 \le N_{Bag} \le 34{,}985$ for our experiments (Fig. 12a). Thus, collisional stresses were dominant over viscous fluid stresses in all subsets, which is typical for natural coarse-grained flows (Lanzoni et al., 2017) and partly valid for other natural debris flows (Iverson and Denlinger, 2001). However, some Bagnold numbers were high in our experiments, especially for flows with large particle diameter compared to flow depth or for rapid and shallow flows resulting in high shear rates. By using Eq. (C.4), our values for the Bagnold numbers range between $201 \le N_{Bag} \le 13{,}804$, which confirms the domination of the collision stresses. This is in comparison with small-scale experimental results (de Haas et al., 2015; Sanvitale and Bowman, 2017) and with large-scale experiments in the USGS flume (Iverson, 1997). Nevertheless, Iverson (1997) also lists Bagnold numbers between $0.2 \le N_{Bag} \le 4$ for natural debris flow events, in which grain collision is negligible compared to the influence of viscosity. However, these values are subject to scrutiny because α_s, μ, $\dot{\gamma}$ and d are hard to determine accurately, even in a laboratory experiment due to mixing, phase-separation, changing solid volume fraction, velocity shearing through depth, to name a few.

We evaluated **friction numbers** between $984 \le N_{fric} \le 4987$ for the smooth surface and $1359 \le N_{fric} \le 21{,}854$ for the rough surface (Fig. 12b). In general, the friction forces overruled the viscous forces in our experiments. Importantly, due to the simplified definition of $\dot{\gamma}$, the friction number is proportional to the squared flow depth, and additionally inversely proportional to the flow velocity. Thus, the value dropped conspicuously for shallow and rapid flows with high water content. On the contrary, flows over a rough bed with relatively high solid volume fraction (α_s=0.51) facilitated thicker and slower debris motion, resulting in the highest friction numbers. This wide range of flow types represents well natural flow characteristics (Iverson, 1997; Zhou and Ng, 2010; Lanzoni et al., 2017).

Due to the fact, that solid and water density were constant in our experiments, the **mass number** is only a function of the solid volume fraction. Because α_s was in the range of natural debris flows, the mass numbers had comparable values in the range between $1.984 \le N_{mass} \le 3.227$ (Fig. 12c). As expected, the solid inertia was noticeably higher as the fluid inertia.

Our values for the **Darcy number** ranged between 6 and 317 and were rather low compared to natural debris flow events with fine particle content and other experiments. That means that pore fluid had very low potential to buffer grain interaction and excess pore pressure is negligible. But, that is reasonable due to the lack of fine particles in our experiment, which is confirmed by a similar range for the Darcy number in natural coarse-grained debris flows (Lanzoni et al., 2017).

This also affects the **Stokes number**, which was in the range of $13 \le N_{St} \le 630$ in our experiments. We conclude, that our flow follows generally an accelerated motion and the fluid drag is negligible. The **Froude number** is in the range of $1.0 \le Fr \le 8.4$ in our experiments (Fig. 12c) and are therefore comparable to natural flows (Gray et al., 2003; Evans et al., 2009; Pudasaini and Domnik, 2009; Domnik and Pudasaini, 2012; Arai et al., 2013; Turnbull et al., 2015). High Froude numbers occurred particularly in shallow and rapid flows, mainly in the smooth basal subsets. Lower values were observed in relatively slow flows over the rough surface, especially for coarse particle and α_s=0.51, where the flow was even in critical condition. The **Reynolds numbers** were close to natural conditions in our experiments and were between $1.4 \cdot 10^5$ and $5.0 \cdot 10^5$ (Fig. 12b). However, natural coarse-grained flows show rather lower values for the Reynolds number. The fluid viscosity of pure water was low in our experiments and viscous shearing could barely have a major influence. The **particle Reynolds number** had values between 1681 and 17,884. The values were in particular high, for (i) flows with low water content and therefore largely reduced viscous shearing, (ii) rapid and thin surges resulting in high shear rates and (iii) subsets with large particle sizes. Overall, in all experiments, the solid inertial stress had been dominating viscous shearing stress. Compared to natural debris flows (Table 3 right column), the particle Reynolds numbers in our experiment were noticeable higher, but lay in the range of natural coarse-grained flows (Lanzoni et al., 2017).

Takahashi (2014) concluded, that two types of debris flows exist in the wider sense; a quasi-static flow in which Coulomb frictional stress dominates (small N_{Sav}) or dynamic debris flow (high N_{Sav}). The experiments from this study show relatively high Savage numbers, mainly in collision dominated regimes and only partly in friction dominated regimes (Fig. 12a). Following Takahashi (2014), our experimental flows have to be classified as dynamic debris flows. Moreover, three types of dynamic debris flows can exists (Takahashi, 2014): stony debris flows, dominated by grain collision stresses (large N_{Bag}); turbulent-muddy debris flows, controlled by turbulent mixing stresses (large Re); and viscous flows, dominated by viscous stresses (small N_{Bag} and Re). Our experiments show very large Bagnold numbers (Fig. 12a), but Reynolds number were comparable to natural flows (Fig. 12b). Thus, the flows from this study are stony debris flows, in which the interstitial water have less content of fines and the excess pore fluid pressure will dissipate rapidly from the relatively coarse debris matrix (Hotta, 2011; Kaitna et al., 2011; Stancanelli et al., 2015). Furthermore, by following the occurrence criteria of various type flows on non-cohesive coarse sediment bed (Takahashi, 2014), our experiments are characterised by fully mature debris flows and we can assume, that the particles are dispersed densely in the entire depth. Overall, the dimensional analysis highlights that the performed experiments and natural coarse-grained flows with low muddy-viscous fluid as presented in Lanzoni et al. (2017) are quite similar on dynamic scales. On the contrary, natural debris flows with high muddy-viscous fluid can only be partly mirrored by the experiments of this study.

6. Grouping and classifying the flows

Our experiments reveal that basal roughness, particle size and solid volume fraction have a major influence on flow evolution and overall flow dynamic. In almost all experiments, the debris flow accelerated at first mainly due to higher hydraulic pressure gradients and gravity until the motion had been substantially controlled by overall opposing forces like basal friction, grain collision or drag. For all particle sizes, we found that the more water had been in the debris flow the more chaotic and unpredictable was the flow behaviour. This is confirmed exemplary in natural debris flows reported by Kean et al. (2013) (Videos S4, S5, S6), where an increase in rainfall intensity directly affects the surge velocity and overall flow dynamics. Our data depict that basal friction force will eventually hinder the flowing sediment from gaining speed, in particular, for rough basal conditions. Henceforth, flowing mass was in almost steady or quasi-steady motion, mainly almost at the end of the flume, featuring a nearly constant velocity. However, even if our spectrum of the initial and boundary conditions were very narrow and we concentrated on landslide-induced stony debris flows, the structures and profiles of the moving particle-fluid mixtures evolve differently. We observed many typical natural debris flow properties in our experiments, like phase separation (de Haas et al., 2015; Pudasaini and Fischer, 2020b), head-body diversion with a coarse-grained front followed by dilute material (Takahashi, 1983; Zanuttigh and Lamberti, 2007; Johnson et al., 2012), or precursory surges (Hungr, 2005; Turnbull et al., 2015). Interestingly, these flow properties did not only occurred in multiple subsets with different parameter combinations but can also be linked to a few types of natural flow-like mass movements (Hungr et al., 2001). Therefore, we group the subsets with similar flow properties and arranged them according to their particle size, solid volume fraction, and basal roughness in Table 4. Each of the resulting three groups has such individual flow properties that we could finally assign them to the natural flow-like mass movements: (1) debris flood (hyperconcentrated flow), (2) debris flow with head-body architecture, and (3) non-liquefied debris flow. We display the three observed flow types for different dimensionless numbers in Fig. 12. For each flow type, we complement Table 4 with characteristic figures for flow depth, front position over time, debris front velocity and front shape, as well as the most crucial dimensionless parameters like Froude number, Bagnold number (Bagnold, 1954), Savage number and friction number, separated for both roughnesses. It is worth to mention, that we could not link the observed flow properties to the flow type of (a) sand flow slide, because no significant excess pore-pressure existed in our experiment; (b) clay flow slide, peat flow, earth flow, or mud flow, because of the lack of fine and cohesive material in our grain matrix; (c) debris avalanche, because our setup features a confinement in form of a channel and the experiment did no begun with a shallow surficial sliding failure; (d) rock avalanche, because our sediment matrix did not include such large boulders or fragmented rocks from a rock slide or collapse as a rockfall as a semi-coherent flowing mass.

6.1. Debris flood/hyperconcentrated flow

A debris flood is a very rapid, surging flow of water (the water column is heavily charged with sediments) with velocities similar to water floods and high turbulence. The debris flood can transport comparable quantities of sediment as debris flows in form of, partly multiple, massive surges, mainly propelled by the tractive force of the water (Hungr et al., 2001). Compared to debris flow, a debris flood generates no levees or a significant longitudinal sorting with meaningful coarse-grained fronts. In contrast, debris floods or hyperconcentrated flows, as Pierson (2005) named these phenomena, show a steep water-surface slope, often describes as fast-moving “wall” of debris. Depending on the debris composition and the solid volume fraction, the mass flows form series of surges or roll waves with periods ranging from a few seconds to hours (Takahashi, 1983; Costa, 1984; Jakob and Hungr, 2005; Arai et al., 2013; Takahashi, 2014).

We observed very rapid and highly turbulent flows in subsets with very fine and fine particles (Table 4 first row). The solid volume fraction in these subsets was particular low ($0.43 \le \alpha_s \le 0.47$) and around the threshold of Fleischer (2012). For these flows, the flow depth sensors recorded a very steep surge front followed by a very thin sediment layer. Thus, the majority of the mobilized sediment was agglomerated in the rapid moving frontal surge, what looks like a fast-moving “wall” (Pierson, 2005). However, no longitudinal sorting due to phase-separation was observable. The high water content had a major influence on the flow velocity, which resulted in the largest, observed Froude numbers when flows with same basal roughness are compared (Table 4 eighth column). Compared to the flow over the smooth surface (Fig. 13a), the surge front had been substantially slowed down on the rough surface due to higher basal roughness after disembarking the reservoir (Fig. 13b). But, after the water may had filled up the gaps between the coarse particles and formed a lubricating layer along the flume surface, the internal and basal friction was dynamically reduced for the material which had tailed the first surge (Pudasaini and Krautblatter, 2014). With nearly the momentum as of the frontal surge, the following material sometimes pushed the front from behind, reactivated motion and enhanced the front depth additionally, until it overtopped or breached through the front (Fig. 13b), which can be observed in real debris flows (Bryant, 2005; Turnbull et al., 2015). In general, the front accelerated continuously during downhill motion,

Table 4

Observed flow types in this experimental study related to solid volume fraction α_s, particle size, relevant dimensionless numbers, basal roughness (SS: smooth surface, RS: rough surface) and the representative outcome for flow depth, front velocity and front shape in time. The Bagnold number is calculated referred to Bagnold (1954).

Flow architecture	Flow depth	Front velocity	Front shape	N_{fric}	N_{Sav}	N_{Bag}	Fr	Roughness	α_s	Particle size
Debris flood/hyperconc. flow	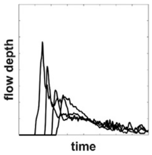	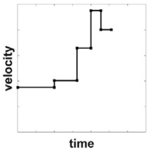	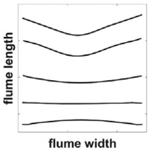	984–1565	0.41–1.52	1780–5587	7.4–8.4	SS	0.43 0.47 0.43	V. fine V. fine Fine
				4640–8781	0.02–0.12	560–1773	3.0–4.3	RS	≤0.47 0.43	V. fine Fine
Debris flow/head-body architecture	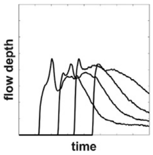	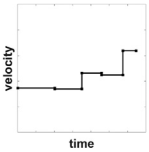	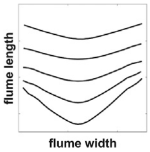	2191–3031	0.18–0.76	1407–4618	5.7–6.7	SS	0.51 0.47	V. fine Fine
				1359–8466	0.06–3.13	1273–18,409	2.4–3.3	RS	0.51 0.47 0.43	V. fine Fine Coarse
Non-liquefied debris flow	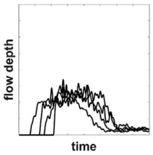	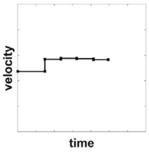	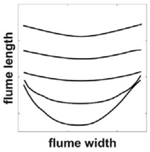	2046–4987	0.23–6.75	1416–34,985	3.7–5.4	SS	0.55 ≥0.51 ≥0.43	V. fine Fine Coarse
				5445–21,854	0.01–0.68	784–10,381	1.0–2.3	RS	0.51 ≥0.47	Fine Coarse

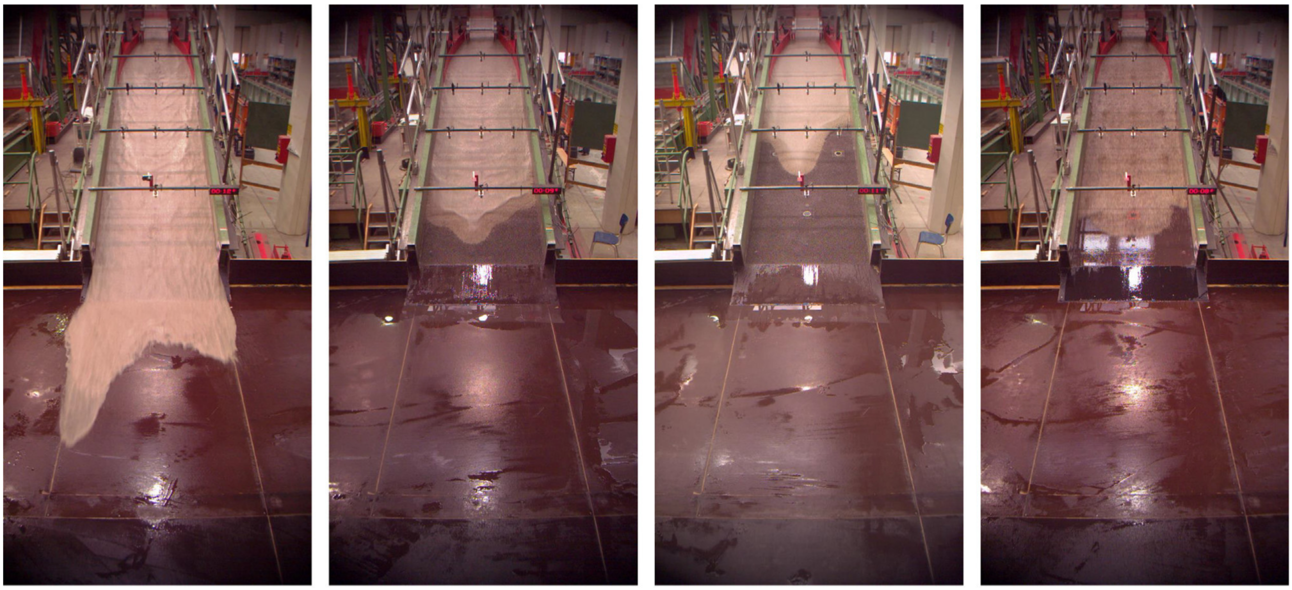

(a) A debris flood (hyperconcentrated flow) on a **smooth surface** for **very fine particles** and $\alpha_s = 0.43$

(b) A debris flood on a **rough surface** with precursory surge for **fine particles** and $\alpha_s = 0.43$

(c) A debris flow with head-body architecture on a **rough surface** for **fine particles** and $\alpha_s = 0.47$

(d) A non-liquefied debris flow on a **smooth surface** for **coarse particles** and $\alpha_s = 0.47$

Fig. 13. Four examples of observed flow types in different subsets: a debris flood (hyperconcentrated flow) on smooth surface, as well as on rough surface, a debris flow, and a non-liquefied debris flow.

resulting in a nonlinear relationship of front position over time. Even if the front shape was rounded after the mixture disembarked the reservoir, the debris flowed down the flume roughly with a flat front, equally distributed over the flume's width (e.g. Fig. 11a,b). The flow was dominated by collisional forces with a Bagnold number larger than 560. The Savage numbers were also rather high, showing that the flow dynamics is affected by grain collision stresses for subsets with the smooth bed. In subsets with the rough bed, the basal friction gain important influence, hindered the flow to achieve similar flow speed, which reduced the Savage number below the threshold. Especially smaller particles caused larger friction due to their effective larger area of contact. The smaller the particles were, the more they had established contact with each other and sheared on the neighbours or basal surface. Opposed to that, lubrication was increased between larger particles, and between particles and the basal surface, because larger particle gaps reduce the basal area of contact. This resulted in a larger velocity. However, the friction numbers in the subsets with the rough bed lay above the threshold of friction dominated flows ($N_{fric} \geq 2000$), showing that in these flows the friction gain some influence compared to viscous forces.

6.2. Debris flow with head-body architecture

A debris flow is a very rapid flow of saturated debris material in a steep channel with the presence of a certain degree of rough longitudinal sorting due to phase-separation (Costa and Williams, 1984; Pudasaini and Fischer, 2020b). Boulders or more dry coarse material will accumulate near the front of the surge and the front may be bypassed by a more dilute body and hyperconcentrated tail. This longitudinal structure is also called head-body architecture (Turnbull et al., 2015). The water content is highly variable in the longitudinal direction due to heterogeneity and transition from dense and coarse-grained surge front and more diluted intersurge flow. When flowing in a channel, steady-state debris flow normally forms a distinguished rounded flow front due to shearing stress at the lateral boundaries. The coarse-grained front might shoulder aside granular material and form noticeable levees which can narrow the effective channel width and enhance the momentum of the flow due to increased velocity. Debris flow usually contains fine (cohesive) sediment to some extent. However, in regions with unweathered crystalline or metamorphic rocks, debris flow can be produced as a coarse particle-fluid mixture with a lack of a silt clay fraction (Hungr et al., 2001).

In our experiments with fine particles and medium solid volume fractions, as well as for subsets with coarse particles and low solid volume fraction (Table 4 second row), the flow dynamics were characterised by a distinguished coarse-grained front, which was followed by a dilute body (Fig. 13c). This longitudinal sorting was mainly influenced by phase-separation, which is similar to those documented for natural debris flows (Takahashi, 1983; Turnbull et al., 2015). The flow depth evolution showed a rather steep debris front, followed by a small part of dilute material with lower flow depths, before a second enhanced, but more rounded peak occurred. Flow velocities slightly increased during downhill motion. The front shape was rounded with a prominent lobe in the channel centre. In some subsets, the front shouldered aside the grains and form gentle levees. These experimentally generated flows mirror well the natural debris flow surges at the Chalk Cliffs in the case of low rainfall intensity, which are documented in Video S4 in Kean et al. (2013). The Froude numbers in our experiments showed clear supercritical flow conditions with values between 2.4 and 6.7. With Bagnold numbers larger than 1200, the collision forces dominated the flows related to this dimensionless number. However, we note, that it depends on how well the shear rate can be approximated. The Savage number shows, that a head-body architecture can develop with dominating Coulomb friction for small particles or with grain collision as the main influence for medium and large particles. The friction numbers reveal also a clear influence in the flow compared to viscous forces.

6.3. Non-liquefied debris flow

A non-liquefied debris flow is a flow-like movement of loose dry or moist, sorted or unsorted granular material without significant excess of pore-pressure. It has a limited velocity, but which depends highly on the flume inclination. The flow may form steep delta fronts (Hungr et al., 2001). If the flow is moving rather slow as a compact homogeneous mixture, one might call it slow moving dense flows.

A dense sliding architecture of the particle-fluid mixture occurred mainly for flows with high solid volume fractions, and either coarse particles, or very fine particles (Table 4 third row). A flow example is presented in Fig. 13d. But, also flows with fine particles and medium solid volume fraction showed a dense motion. The flow motion was quite slow and followed a steady motion in the longitudinal direction. The flow evolution had typically a rounded profile without meaningful longitudinal sorting. The mixture slides down the flume with nearly constant speed and formed prominent snouts, especially for very fine particles, as also observed in experiments from de Haas et al. (2015). The Froude number is spread over a large range for these subsets, depending mainly on the basal roughness. On the rough surface, the Froude number was low and at the limit for supercritical flow. The particle-fluid interaction was dominated by collisional forces ($N_{Bag} \geq 450$). The Savage number showed mainly values above 0.1, so collisional forces overruled Coulomb frictional forces. However, on the rough surface, some flows with high solid volume fraction showed noticeable lower values than the threshold presented by Savage and Hutter (1989). Here, the Coulomb friction demonstrated meaningful influence. The friction number shows, that frictional forces overruled viscous forces for the rough surface. Due to the calculated bulk density profiles (Fig. 9), we assume, that all regions of our dense flows were still in nearly saturated conditions during motion and cannot be classified per se as non-liquefied debris flows. However, the observed flow properties fit best in that flow type.

7. Conclusions

Gravity-driven mass flows often appear as a mixture of fluid and solid particles and are very difficult to predict. Their flow evolution crucially depends on a variety of alterable initial and boundary conditions as well as on their intrinsic interactions during the motion. Different flow types describe the varying flow dynamics and structures of the flow. To study the flow evolution, many experiments have been conducted, investigating the influence of individual parameters, like slope, grain size distribution, solid volume fraction, or content of fines, to name only a few. This study aimed to concentrate only on landslide-induced stony debris flows and to investigate the flow evolution in a narrow parameter spectrum of basal roughness, solid volume fraction, and grain size. We were looking for characteristic properties of common flow types in our experiments and compare them with dimensionless quantities and flow characteristics of natural events with a coarse-grain matrix. Furthermore, we aimed to deepen the knowledge about coarse-grained particle-fluid mixture flows as a niche of debris flow and aimed to provide new extensive data set from well-controlled laboratory experiments for the calibration and validation purpose of numerical approaches.

We conducted 72 experiments and measured the flow depth, the flow mass, the front velocity, and the shape of the debris front with varying particle sizes, basal roughness and solid volume fractions. Out of flow depth and mass, we evaluated the depth-averaged bulk density, which gave a good indication about the evolution of the bulk density but reacted sensitively to very low flow depth values. In our experiments, initial solid volume fraction and basal roughness had a significant influence on flow variables, such as flow depth, velocity, and front shape and the resulting flow evolution. In the half of our experiments, the initially prepared homogeneous particle-fluid mixtures were sliding down the flume as a rather dense mass, especially for high solid volume fractions. In other cases, especially on a smooth bed, shallow and rapid flows resulted in highly turbulent flows and sometimes debris front overtopping. For rough beds, the flow evolution was governed by dilute flows with coarse-grained debris fronts and longitudinal sorting. Lower layers of these flows might be noticeably hindered in motion by high basal friction because grains in the higher layers reaching the flow front and tumbles down to the bottom and were buried in the flow head again. This highlights the associated segregation and phase separation phenomena. The particle-fluid mixture flow later re-accelerated by a dilute debris body pushing the front from behind. Overall, our results reveal, that small changes in solid volume fraction, as well as the basal roughness, strongly govern the evolution of the flow depth and the velocity of the flow. On the contrary, the particle size has a substantial effect on the debris front shape and its evolution during downhill motion. Larger particle ran faster in subsets with the same solid volume fraction, but these flows exhibit lower front surges.

Several dimensionless numbers were considered and calculated to determine the acting flow regimes and to discuss the transferability of our experiments to natural events and other experimental data. In our experiments, the flow was generally in a supercritical flow regime. Grain collisional stresses dominated our experimental flows, which is also the case in natural stony debris flows. Frictional forces gain some influence for flows over the rough surface, in particular for low solid volume fractions. Due to the lack of high viscous fluid, collisional stresses were dominant over viscous fluid stress in all of our subsets. Besides, friction forces overruled viscous forces in all experiments.

Interestingly, even if we concentrated on landslide-induced stony debris flows and keep our parameters in a narrow spectrum, we could still observe different flow properties. These properties allowed us to group the observed flows regarding their flow properties and assign them roughly to common categories of three natural flow-like mass movements: (1) debris flood (hyperconcentrated flow), (2) debris flow with head-body architecture, and (3) non-liquefied debris flow. Although we could mirror these flows in respect, our flow conditions were simplified compared to natural conditions, e.g., by using mixtures of nearly spherical particles and tap water, which do not fully represent the wide range of particle sizes and the non-Newtonian behaviour of the interstitial fluid in natural flows. We only observed bulk-flow behaviour and had no information about the velocity distribution in the debris column. However, the outer structures of the different flows were somehow sufficient to group them into different flow types. Moreover, for simplification, we kept the inclination of the flume constant in all experiments and used a non-erodible bed. However, we investigated the impact of the basal roughness by mounting a smooth and later a rough surface in the flume. A further limitation of this study includes the absence of cohesive particles and high viscous fluid in the debris sediment mixture, or the missing erodible boundaries like banks and beds. There is some proof in the values of the pressure number, that in our flows excess pore pressure may not be developed, in contrast to the most natural flow, where a non-hydrostatic fluid pressure has usually a major influence. Furthermore, morphodynamics is expected to vary noticeably if sediment transport takes place in a nature-orientated curved terrain. Nevertheless, we present a large number of well-controlled experiments with a focus on two-phase particle-fluid mixtures for landslide-induced stony debris flows under a largely varying initial and boundary conditions. The results give new profound insights into the causal relationship between these conditions, the parameter of flow dynamics (flow depth, flow mass, bulk density, velocity, front shape), and their effects on the flow types. We plan to present the deposition results from this study in an upcoming publication.

Declaration of competing interest

The authors declare that they have no known competing financial interests or personal relationships that could have appeared to influence the work reported in this paper.

Author Contribution: Ivo Baselt evaluated the data and compiled the manuscript. Gustavo Q. de Oliveira conducted the experiments. Jan-Thomas Fischer and Shiva Pudasaini supervised the manuscript and the project.

Acknowledgements

The experiments were embedded in a transnational research project, which connects researchers from Germany and Austria. The group developed the GIS-based open-source simulation tool r.avaflow (www.avaflow.org) for modelling general avalanche and debris flows over natural topography. The work presented in this paper has been financially supported by the German Research Foundation (DFG) through the research project, PU 386/3-2 and KU 3126/2-1: "Development of a GIS-based Open Source Simulation Tool for Modelling General Avalanche and Debris Flows over Natural Topography" within a transnational research project, D-A-CH. We are deeply grateful for many productive discussions within the project group, in particular with Prof. Dr.-Ing. Andreas Malcherek. We thank the staff of the Hydraulic Laboratory for their outstanding performance in constructing and maintaining the setup. We would like to address special thanks to Dr.-Ing. Helmut Kulisch, who contributed extensively in the construction of the experimental setup, but sadly passed away during the project. We thank the anonymous reviewers and the Editor Markus Stoffel for many helpful comments that improved this manuscript.

Appendix A. Sediment categories

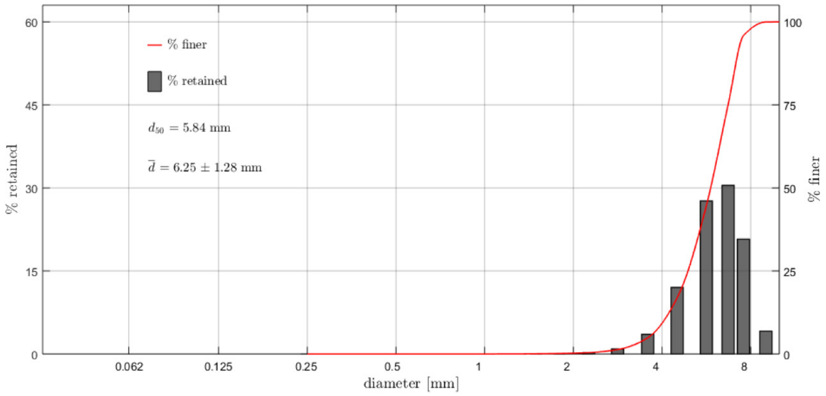

(a) coarse particle (gravel)

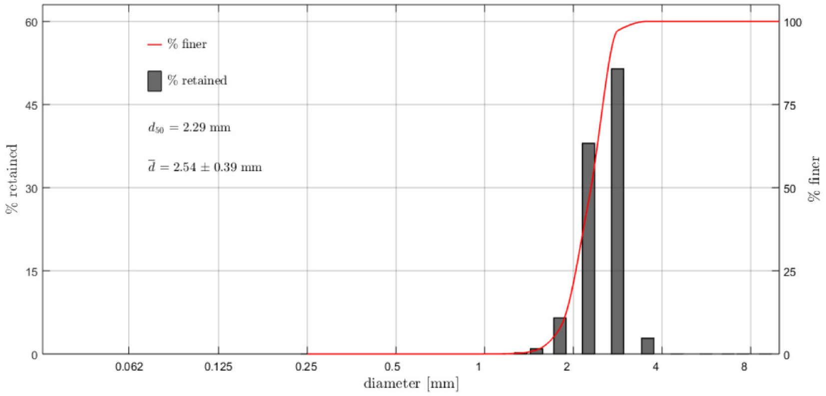

(b) fine particle (gravel)

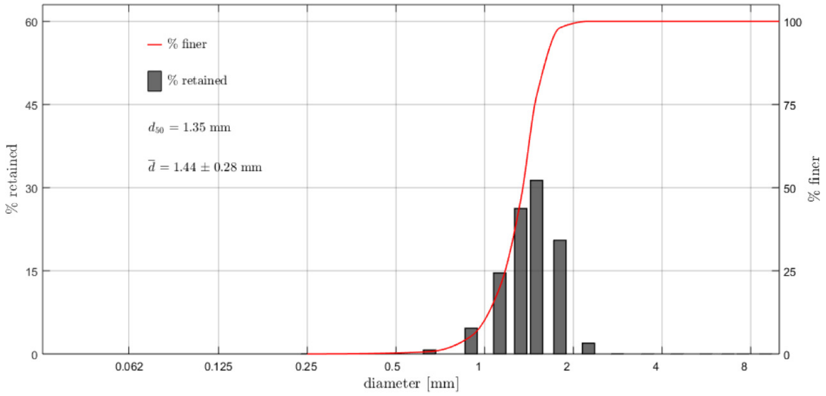

(c) very fine particle (sand)

Fig. A.14. Used sediment categories for coarse, fine, and very fine particles with the particle-size distribution curve.

Appendix B. Results from unsteady conditions on the smooth surface and α_s=0.43

The subsets for α_s=0.43 and smooth surface are generally characterised by a highly turbulent and rapid flow. The low solid volume fraction facilitated an acceleration of the flow, which can be seen in the diminishing time intervals between the triggering events of two neighbouring sensors (Fig. B.15a, b). The time intervals increase with the solid fraction. For α_s=0.51, the time intervals are even similar, showing a roughly steady-state motion (Fig. B.15c). The amount of water in the released mixture affected also the debris height. The hydrographs for very fine particles show steep and sharp debris fronts observable in every sensor location. The prominent front spike diminished for larger grains. No debris front peak was observed for coarse particles, even if the solid volume fraction was very low. Comparing the flow depth in lateral directions also highlights that the debris front reached the centre position a bit before the lateral positions. However, this time delay is rather marginal because the front shapes developed into a relatively straight profile over the flume width in particular in the second half of the flume. To achieve quasi-steady conditions also with such low solid volume fractions, we assume that the flume should have been at least twice as long. However, this is not easy in common laboratories.

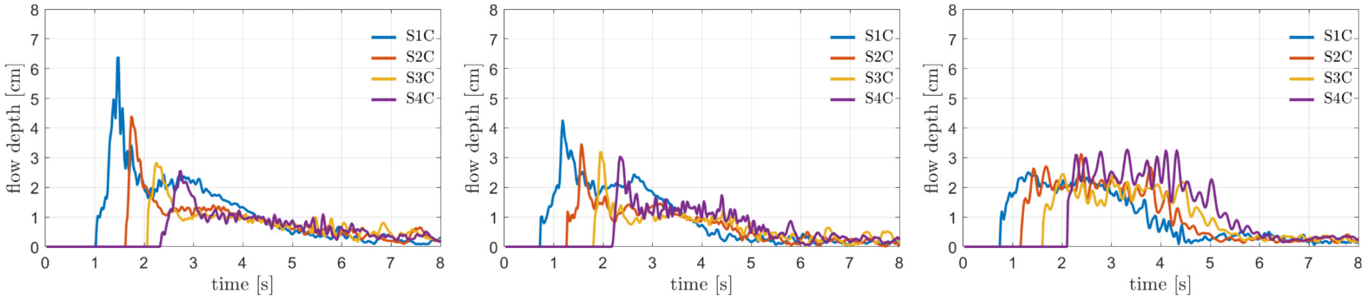

(a) smooth s., very fine particles, $\alpha_s = 0.43$ (b) smooth s., fine particles, $\alpha_s = 0.43$ (c) smooth s., coarse particles, $\alpha_s = 0.43$

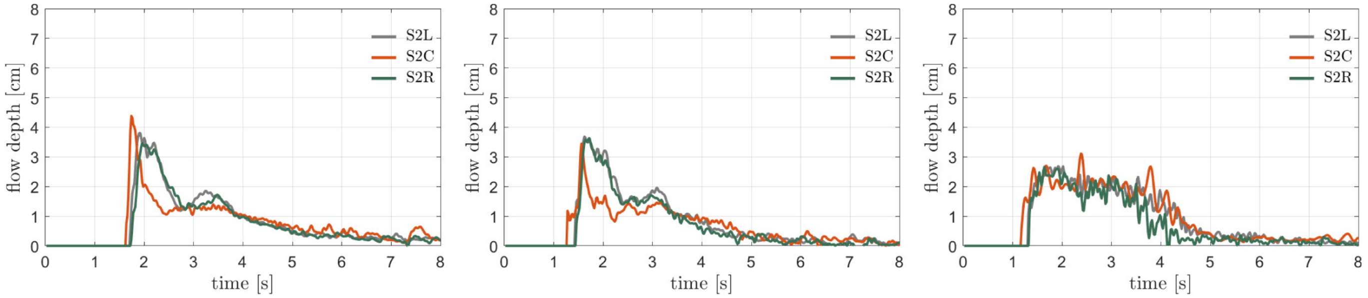

(d) smooth s., very fine particles, $\alpha_s = 0.43$ (e) smooth s., fine particles, $\alpha_s = 0.43$ (f) smooth s., coarse particles, $\alpha_s = 0.43$

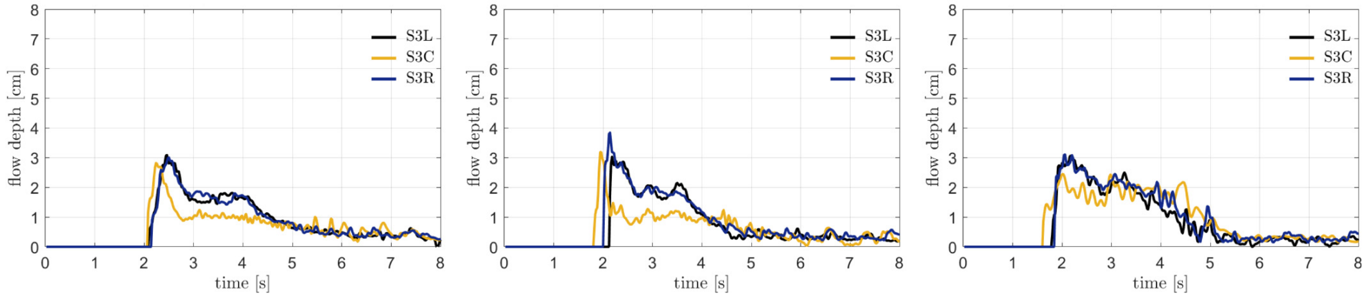

(g) smooth s., very fine particles, $\alpha_s = 0.43$ (h) smooth s., fine particles, $\alpha_s = 0.43$ (i) smooth s., coarse particles, $\alpha_s = 0.43$

Fig. B.15. Flow depth measurements for the unsteady conditions on the smooth surface and α_s=0.43.

Appendix C. Dimensionless numbers

C.1. Pressure number

Pore fluid and fluid pressure play an important role in debris flow dynamics and it is the chief mechanical agent to divide debris flow from granular avalanches (Takahashi, 1991; Pitman and Le, 2005; Iverson et al., 2010; Pudasaini, 2012). A relation between the timescale for downslope flow and pore pressure diffusion is expressed by the dimensionless pressure number

$$N_p = \frac{\sqrt{L/g}}{h^2/D}, \tag{C.1}$$

taking into account a typical flow length L, the flow depth h, and the hydraulic diffusivity D (Iverson and Denlinger, 2001; de Haas et al., 2015). de Haas et al. (2015) assumed that the flow length L is equal to the channel length. But, it might be reasonable to take only half the channel length for our experiments because in most cases debris flow had covered only this part in the runs. The pressure number assumes values $N_p \ll 1$ in most natural geophysical flows, where a high pore pressure persists much longer in the flow than the grain flow needs to move downslope (Iverson and Denlinger, 2001; Zhou and Ng, 2010).

C.2. Savage number

A gravity-driven particle-fluid mixture flow, which is influenced by Coulomb friction and grain collision, can be evaluated by using the Savage number (Savage and Hutter, 1989; Parsons et al., 2001)

$$N_{Sav} = \frac{\rho_{solid}\dot{\gamma}^2 d_{mean}^2}{(\rho_{solid}-\rho_{water})gh\ \tan\phi\ \cos\theta}, \tag{C.2}$$

as the ratio of grain collision stresses and gravitational grain contact stresses (Iverson and Denlinger, 2001). For the internal angle of friction ϕ, the determined values from Table 1 were used. In the numerator, $\dot{\gamma} = v/h$ is the shear rate of the flow, which was approximated by the free surface surge velocity and the flow height of the front (Zhou and Ng, 2010). A flow with a very high grain concentration, like in our experiments, induce frequent collision of particles resulting in a momentum transfer between neighboured grains (Takahashi, 1983). Savage and Hutter (1989) inferred that the flow dynamics at typical depths is significantly affected by grain collision stresses if $N_{Sav}>0.1$. Iverson and Denlinger (2001) listed values between $0.001 \le N_{Sav} \le 0.2$ for well-documented geophysical events and deduced that many natural flows are probably dominated by friction rather than by grain collisions. Zhou and Ng (2010) reported values roughly between $10^{-5} \le N_{Sav} \le 6 \cdot 10^{-2}$. For small-scale experiments, de Haas et al. (2015) calculated Savage numbers between $0.17 \le N_{Sav} \le 2.25$ and Sanvitale and Bowman (2017) determined values roughly between $10^{-3} \le N_{Sav} \le 10^{2}$.

C.3. Bagnold number

To compare grain collision stresses and viscous fluid stresses in a particle-fluid mixture flow with interstitial Newtonian fluid, Bagnold (1954) presented a dimensionless number

$$N_{Bag} = \left(\frac{\alpha_s^{1/3}}{\left(\alpha_{s,\,\max}^{1/3} - \alpha_s^{1/3}\right)} \right)^{1/2} \frac{\rho_{solid} \dot{\gamma} d_{mean}^2}{\mu}, \tag{C.3}$$

known as the Bagnold number (Iverson and Denlinger, 2001). Both, the bulk normal and the shear stresses in a steady, uniform shear flow are proportional to the shear rate if the Bagnold number falls below roughly 40. A flow is dominated by collisional forces with Bagnold numbers higher than roughly 450, in which bulk normal and shear stresses are proportional to $\dot{\gamma}^2$ (Iverson and Denlinger, 2001). Dullien (1991) specifies the maximum solid volume fraction of a densest regular-packed granular sphere-shaped sediment as $\alpha_{s,\,max}=0.7405$. Among others, de Haas et al. (2015) and Sanvitale and Bowman (2017) used the modified Bagnold number derived by Iverson (1997)

$$N_{Bag} = \frac{\alpha_s}{(1-\alpha_s)} \frac{\rho_{solid} \dot{\gamma}\, d_{mean}^2}{\mu}, \tag{C.4}$$

to evaluate their small-scale experiments. The Bagnold number threshold for collision dominated flows is roughly 200 with that approach.

C.4. Friction number

Another dimensionless number can be obtained by defining a ratio of Bagnold number (C.4) and Savage number (C.2) (Iverson and LaHusen, 1993). Named as friction number, it is the quotient of frictional to viscous forces (Iverson, 1997; de Haas et al., 2015)

$$N_{fric} = \frac{\alpha_s}{(1-\alpha_s)} \frac{(\rho_{solid} - \rho_{water}) gh \tan\phi \cos\theta}{\mu \dot{\gamma}}. \tag{C.5}$$

Researchers constrain different magnitudes of this number for the transition between friction and viscous dominated states in a flow. A well-accepted threshold for friction dominated flows is $N_{fric}>2000$ (Bagnold, 1954; Savage and Hutter, 1989). In contrast, Parsons et al. (2001) suggest lower thresholds of $N_{fric}>100$ for the debris body or $N_{fric}>250$ for the flow front in water-saturated flows. The flows in the USGS-experiments reached values of 2000–3000, but natural flows usually have noticeable enhanced friction numbers up to 10^9 (Iverson, 1997; Iverson and Denlinger, 2001; Zhou and Ng, 2010). de Haas et al. (2015) estimated the values $141 \le N_{fric} \le 2760$ for their small-scale experiments, partly owned by explicit viscous mud flows due to the use of particles and sand.

C.5. Mass number

The mass number describes the ratio of solid inertia to fluid inertia in the mixture (Iverson, 1997), which is dependent on the density and the concentration of the solid grains in the flow.

$$N_{mass} = \frac{\alpha_s}{(1-\alpha_s)} \frac{\rho_{solid}}{\rho_{water}} \tag{C.6}$$

The mass number increases if the solid volume fraction rises. Very dilute flows are marked with low values. Theoretically, a wide spectrum from zero to infinity is possible for the mass number. But, values range typically between 1 and 10 in experiments and natural debris flows (Iverson, 1997; de Haas et al., 2015).

C.6. Darcy number

We evaluated the ability of pore fluid pressure to buffer grain interactions by calculating the Darcy number (Iverson, 1997).

$$N_{Dar} = \frac{\mu}{\alpha_s \rho_{solid} \dot{\gamma} k} \tag{C.7}$$

Iverson and LaHusen (1989) conducted experiments along a single slip surface in cylindrical fiberglass rods. Although they did not calculate any Darcy numbers, one can use the tabled static physical properties of the experimental media to calculate them subsequently. By doing so, one found values between $8857 \le N_{Dar} \le 35{,}427$. Iverson and LaHusen (1989) also conducted experiments during rapid shear deformation of realistic geological materials. In their experiments, large fluid pressure fluctuations evidenced strong particle-fluid interactions. With the extracted data from these artificial landslides, Darcy numbers of $N_{Dar}=14{,}060$ and $N_{Dar}=15{,}953$ can be determined. For other experiments Iverson et al. (2010) present $N_{Dar}=600$ and de Haas et al. (2015) calculated values between $3.2 \cdot 10^4 \le N_{Dar} \le 5.9 \cdot 10^7$. Typical ranges in natural flows feature $10^4 \le N_{Dar} \le 10^8$ (Iverson, 1997).

C.7. Stokes number

The Stokes number

$$N_{St} = \frac{1}{18} \frac{\rho_{solid}}{\rho_{water}} \frac{d_{mean}^2 \gamma}{\nu} \tag{C.8}$$

represents the ratio of the time scale of deceleration due to Stokes viscous drag force and the time a grain move a distance of its own mean diameter (Armanini et al., 2005). The Stokes number analyses the effect of the fluid drag on a grain when a relative motion of solid and fluid phase is not negligible (Lanzoni et al., 2017). The flow can be classified by three regimes. A viscous regime occurs for $N_{St} \ll 1$. For $N_{St} \gg \sqrt{\rho_{solid}/(\rho_{water} C_d)}$ with the drag coefficient $C_d \approx 0.4$, and $\sqrt{\rho_{solid}/(\rho_{water} C_d)} \ll 1$, the flow is in a inertial regime. For $N_{St} \gg 1$, the flow is accelerated and the fluid drag is negligible (Du Courrech Pont et al., 2003; Cassar et al., 2005; Lanzoni et al., 2017).

C.8. Froude number

The Froude number characterises the dynamics of free surface gravity flows. It is defined as the ratio between the inertial and gravity forces or equivalently between the kinetic and potential energies (Gray et al., 2003; Domnik and Pudasaini, 2012).

$$Fr = \frac{v}{\sqrt{gh \cos\theta}} \tag{C.9}$$

For Froude numbers less than, equal to, or greater than unity, the flow is in subcritical, critical, or supercritical regime. To include potential energy caused by the gravitational acceleration along the flow depth, and the potential energy caused by the downslope gravitational acceleration in a non-shallow flow with a non-bed-parallel surface over an inclined plane, one should use an extended Froude number (Pudasaini and Domnik, 2009; Domnik and Pudasaini, 2012). Many natural debris flows and granular avalanches are in supercritical regimes (Gray et al., 2003; Evans et al., 2009; Arai et al., 2013; Turnbull et al., 2015). However, in more viscous flows with relatively low flow velocity or comparable large flow depth, the Froude number may reach the subcritical regime (Larcher et al., 2007; Arai et al., 2013; Kailey, 2013; Cageao, 2014). In experimental setups with open channel geometry, the flows are mainly in supercritical regime, because of their rapid and shallow behaviour (Iverson et al., 2010; de Haas et al., 2015; McFall et al., 2018; Wang et al., 2018).

C.9. Reynolds number

Usually, the Reynolds number classifies whether a flow of a Newtonian fluid is laminar or turbulent (Takahashi, 2014). Iverson and Denlinger (2001) and Iverson et al. (2010) derived an analogous Reynolds number

$$Re = \frac{h\sqrt{gL}}{\mu/\rho_{bulk}} \tag{C.10}$$

as a dynamic scaling factor for the normalized momentum equation for flowing debris mixture. Pudasaini (2012) derived a quasi-Reynolds number and mobility Reynolds number for two-phase debris flows. The two length scales h and L are important: h is the typical thickness of the flow and L is the typical flow length in the direction of the flow (Savage and Hutter, 1989). Together with the magnitude of the gravitational acceleration g, the flow length L forms the velocity $\sqrt{gL}$ of a freely falling body (Pudasaini and Hutter, 2007), causing the downslope motion of a debris mass. The Reynolds number has typically values larger than $Re>10^6$ for natural geophysical flow, in particular with large $h\sqrt{gL}$ where the viscous effect will be less important (Iverson and Denlinger, 2001). However, the values in geometrically similar models depend mainly on the scale. A dynamic similarity over a broad range of scales is perhaps unattainable. Too scaled-down debris flows may exhibit disproportionately large effects of viscous flow resistance, which results in smaller Reynold numbers (Iverson et al., 2010). That is the reason to conduct debris-flow experiments at the largest scale possible. The large-scale experiments in the USGS flume featured Reynolds numbers around $1 \cdot 10^5$ (Iverson et al., 2010). The small-scale experiments conducted by de Haas et al. (2015) reveal only values in the range of $2.3 \cdot 10^4$–$1.4 \cdot 10^5$. Both are rather small values compared to natural geophysical flow.

C.10. Particle Reynolds number

The particle Reynolds number

$$Re_p = \frac{\rho_{water} d_{mean} v}{\mu} \tag{C.11}$$

opposes the effects of particle collision and pore fluid viscosity (Iverson, 1997). In principle, it is described as the ratio between the solid inertial stress and the fluid viscous stress (Pudasaini, 2012; de Haas et al., 2015). Vanoni (2006) mentions that fluid start to show inertial effects with respect to the grains in the mixture for $Re_p>1$. Assuming a relatively high fluid viscosity (μ=0.5 Pa s), Zhou and Ng (2010) present flow data with particle Reynolds numbers between roughly 0.1 and 1.6. They mentioned that the most particle Reynolds numbers are below one. They reason, that for natural debris flow, fluid viscous shearing has a significant effect on the mobility. However, the particle Reynolds number is sensitive to a change in the fluid viscosity and a smaller value, μ=0.05 Pa s as suggested by Iverson (1997), is possible likewise. So, the presented flows in Zhou and Ng (2010) could have featured higher particle Reynolds numbers by one order of magnitude, with the solid inertial stress as the dominating effect. In the small-scale experiments from de Haas et al. (2015), particle Reynolds number occurred in the range of $31 \le Re_p \le 504$, indicating high solid inertial stress compared to viscous shearing stress. However, the effective viscosity of fluid may change significantly depending on the yield strength, pressure, and shear rate. This has been shown by Pudasaini and Mergili (2019). So, the above analysis of the Reynolds number and particle Reynolds number must be revisited.

Appendix D. Supplementary data

We provide the graphs as well as the videos in the supplementary available at the journal's website https://doi.org/10.1016/j.geomorph.2020.107431. Supplementary spreadsheet summarizes all data.

References

Ancey, C., Meunier, M., Richard, D., 2003. Inverse problem in avalanche dynamics models. Water Resour. Res. 39, 319. https://doi.org/10.1029/2002WR001749.

Arai, M., Huebl, J., Kaitna, R., 2013. Occurrence conditions of roll waves for three grain–fluid models and comparison with results from experiments and field observation. Geophys. J. Int. 195, 1464–1480. https://doi.org/10.1093/gji/ggt352.

Armanini, A., 2015. Closure relations for mobile bed debris flows in a wide range of slopes and concentrations. Adv. Water Resour. 81, 75–83. https://doi.org/10.1016/j.advwatres.2014.11.003.

Armanini, A., Capart, H., Fraccarollo, L., Larcher, M., 2005. Rheological stratification in experimental free-surface flows of granular–liquid mixtures. J. Fluid Mech. 532, 269–319.

Armanini, A., Fraccarollo, L., Larcher, M., 2008. Liquid–granular channel flow dynamics. Powder Technol. 182, 218–227. https://doi.org/10.1016/j.powtec.2007.08.012.

Bagnold, R.A., 1954. Experiments on a gravity-free dispersion of large solid spheres in a newtonian fluid under shear. Proceedings of the Royal Society A: Mathematical, Physical and Engineering Sciences 225, 49–63. https://doi.org/10.1098/rspa.1954.0186.

Bernard, M., Berti, M., Crucil, G., Simoni, A., Gregoretti, C., 2019. Characteristics of debris flows just downstream the initiation area on Punta Nera cliffs, Venetian Dolomites. In: Kean, J.W., Coe, J.A., Santi, P.M., Guillen, B.K. (Eds.), Debris-flow Hazards Mitigation: Mechanics, Monitoring, Modeling, and Assessment, pp. 557–564.

Bryant, E., 2005. Natural Hazards. Cambridge University Press, Cambridge https://doi.org/10.1017/CBO9780511811845.

Cageao, P.P., 2014. Fluid Particle Interaction in Geophysical Flows: Debris Flows. PhD Thesis. University of Nottingham, Nottingham, UK.

Cassar, C., Nicolas, M., Pouliquen, O., 2005. Submarine granular flows down inclined planes. J. Geophys. Res. 17, 103301. https://doi.org/10.1063/1.2069864.

Cheng, Y.M., Fung, W.H.I., Li, L., Li, N., 2019. Laboratory and field tests and distinct element analysis of dry granular flows and segregation processes. Natural Hazards and Earth System Science 19, 181–199. https://doi.org/10.5194/nhess-19-181-2019.

Costa, J.E., 1984. Physical geomorphology of debris flows. In: Costa, J.E., Fleisher, P.J. (Eds.), Developments and Applications of Geomorphology. Springer, Berlin Heidelberg, Berlin, Heidelberg, pp. 268–317 https://doi.org/10.1007/978-3-642-69759-3_9.

Costa, J.E., Williams, G.P., 1984. Debris-flow dynamics Open-File Report.

de Haas, T., Braat, L., Leuven, J.R.F.W., Lokhorst, I.R., Kleinhans, M.G., 2015. Effects of debris flow composition on runout, depositional mechanisms, and deposit morphology in laboratory experiments. Journal of Geophysical Research: Earth Surface 120, 1949–1972. https://doi.org/10.1002/2015JF003525.

De Oliveira, G.Q., Kulisch, H., Scheidl, C., Fischer, J.T., Pudasaini, S.P., 2015. Tracking of Laboratory Debris Flow Fronts With Image Analysis: EGU General Assembly 2015 (Wien).

De Oliveira, G.Q., Kulisch, H., Malcherek, A., Fischer, J.T., Pudasaini, S.P., 2016. Density Estimation in Laboratory Debris Flow Experiments: EGU General Assembly 2016 (Wien).

Deangeli, C., 2008. Laboratory granular flows generated by slope failures. Rock Mech. Rock. Eng. 41, 199–217. https://doi.org/10.1007/s00603-007-0131-1.

Denlinger, R.P., Iverson, R.M., 2001. Flow of variably fluidized granular masses across three-dimensional terrain: 2. Numerical predictions and experimental tests. Journal of Geophysical Research 106, 553–566. https://doi.org/10.1029/2000JB900330.

Domnik, B., Pudasaini, S.P., 2012. Full two-dimensional rapid chute flows of simple viscoplastic granular materials with a pressure-dependent dynamic slip-velocity and their numerical simulations. J. Non-Newtonian Fluid Mech. 173-174, 72–86. https://doi.org/10.1016/j.jnnfm.2012.03.001.

Du Courrech Pont, S., Gondret, P., Perrin, B., Rabaud, M., 2003. Granular avalanches in fluids. Phys. Rev. Lett. 90, 044301. https://doi.org/10.1103/PhysRevLett.90.044301.

Dullien, F.A., 1991. Porous Media: Fluid Transport and Pore Structure. 2nd ed. Elsevier Science, Oxford URL: http://gbv.eblib.com/patron/FullRecord.aspx?p=1130068.

Egashira, S., Honda, N., Itoh, T., 2001. Experimental study on the entrainment of bed material into debris flow. Physics and Chemistry of the Earth, Part C: Solar, Terrestrial & Planetary Science 26, 645–650. https://doi.org/10.1016/S1464-1917(01)00062-9.

Egli, T., 1996. Hochwasserschutz und Raumplanung: Schutz vor Naturgefahren mit Instrumenten der Raumplanung - dargestellt am Beispiel von Hochwasser und Murgängen. volume 100 of ORL-Bericht. vdf Hochsch.-Verl. an der ETH, Zürich.

Evans, S.G., Bishop, N.F., Fidel Smoll, L., Valderrama Murillo, P., Delaney, K.B., Oliver-Smith, A., 2009. A re-examination of the mechanism and human impact of catastrophic mass flows originating on Nevado Huascarán, Cordillera Blanca, Peru in 1962 and 1970. Eng. Geol. 108, 96–118. https://doi.org/10.1016/j.enggeo.2009.06.020.

Fleischer, G., 2012. Hochwasser und Murgänge in kleinen alpinen Einzugsgebieten–Bedingungen, Ereignisdatenzusammentrag und menschliche Ohnmacht. Hallesches Jahrbuch für Geowissenschaften 32, 113–128 URL: http://public.bibliothek.uni-halle.de/index.php/hjg/article/download/16/23.

Frank, F., McArdell, B.W., Huggel, C., Vieli, A., 2015. The importance of entrainment and bulking on debris flow runout modeling: examples from the Swiss Alps. Natural Hazards and Earth System Science 15, 2569–2583. https://doi.org/10.5194/nhess-15-2569-2015.

Garcia Aragon, J.A., 1995. Granular-fluid chute flow: experimental and numerical observations. J. Hydraul. Eng. 121, 355–364. https://doi.org/10.1061/(ASCE)0733-9429(1995)121:4(355).

Gray, J.M.N.T., 2018. Particle segregation in dense granular flows. Annu. Rev. Fluid Mech. 50, 407–433. https://doi.org/10.1146/annurev-fluid-122316-045201.

Gray, J.M.N.T., Tai, Y.C., Noelle, S., 2003. Shock waves, dead zones and particle-free regions in rapid granular free-surface flows. J. Fluid Mech. 491, 161–181. https://doi.org/10.1017/S0022112003005317.

Gregoretti, C., Stancanelli, L.M., Bernard, M., Boreggio, M., Degetto, M., Lanzoni, S., 2019. Relevance of erosion processes when modelling in-channel gravel debris flows for efficient hazard assessment. J. Hydrol. 568, 575–591. https://doi.org/10.1016/j.jhydrol.2018.10.001.

Hampton, M.A., 1979. Buoyancy in debris flows. Journal of Sedimentary Research 49. https://doi.org/10.1306/212F7838-2B24-11D7-8648000102C1865D.

Hotta, N., 2011. Pore water pressure distributions of granular mixture flow in a rotating mill. In: Italian Journal of Engineering Geology and Environment-Book (Ed.), 5th International Conference on Debris-Flow Hazards Mitigation: Mechanics, Prediction and Assessment. Padua, Italy-14–17 June 2011, pp. 319–330 https://doi.org/10.4408/IJEGE.2011-03.B-037.

Hsu, L., Kaitna, R., Dietrich, W.E., Sklar, L.S., 2011. Boundary shear stress of granular flows. In: Italian Journal of Engineering Geology and Environment-Book (Ed.), 5th International Conference on Debris-Flow Hazards Mitigation: Mechanics, Prediction and Assessment. Padua, Italy-14–17 June 2011, pp. 331–338 https://doi.org/10.4408/IJEGE.2011-03.B-038.

Hungr, O., 2005. Classification and terminology. In: Jakob, M., Hungr, O. (Eds.), Debris-flow Hazards and Related Phenomena. Praxis Publishing Ltd, Berlin, Heidelberg. Springer Praxis Books, pp. 9–23.

Hungr, O., Morgenstern, N.R., 1984. Experiments on the flow behaviour of granular materials at high velocity in an open channel. Géotechnique 34, 405–413. https://doi.org/10.1680/geot.1984.34.3.405.

Hungr, O., Evans, S.G., Bovis, M.J., Hutchinson, J.N., 2001. A review of the classification of landslides of the flow type. Environ. Eng. Geosci. 7, 221–238. https://doi.org/10.2113/gseegeosci.7.3.221.

Hungr, O., Leroueil, S., Picarelli, L., 2014. The Varnes classification of landslide types, an update. Landslides 11, 167–194.

Hussin, H.Y., Quan Luna, B., van Westen, C.J., Christen, M., Malet, J.P., van Asch, T.W.J., 2012. Parameterization of a numerical 2-D debris flow model with entrainment: a case study of the Faucon catchment, Southern French Alps. Natural Hazards and Earth System Science 12, 3075–3090. https://doi.org/10.5194/nhess-12-3075-2012.

Hutchinson, J.N., 1988. General report: morphological and geotechnical parameters of landslides in relation to geology and hydrogeology. Proceedings of 5th International Symposium on Landslides, Balkema, Rotterdam, Netherlands, 1988 , pp. 3–35 URL: https://ci.nii.ac.jp/naid/10029739459/en/.

Iverson, R.M., 1997. The physics of debris flows. Rev. Geophys. 35, 245–296. https://doi.org/10.1029/97RG00426.

Iverson, R.M., 2005. Debris-flow mechanics. In: Jakob, M., Hungr, O. (Eds.), Debris-flow Hazards and Related Phenomena. Praxis Publishing Ltd, Berlin, Heidelberg. Springer Praxis Books, pp. 105–134.

Iverson, R.M., 2015. Scaling and design of landslide and debris-flow experiments. Geomorphology 244, 9–20. https://doi.org/10.1016/j.geomorph.2015.02.033.

Iverson, R.M., Denlinger, R.P., 2001. Flow of variably fluidized granular masses across three-dimensional terrain: 1. Coulomb mixture theory. Journal of Geophysical Research 106, 537–552. https://doi.org/10.1029/2000JB900329.

Iverson, R.M., LaHusen, R.G., 1989. Dynamic pore-pressure fluctuations in rapidly shearing granular materials. Science (New York, N.Y.) 246, 796–799. https://doi.org/10.1126/science.246.4931.796.

Iverson, R.M., LaHusen, R., 1993. Friction in debris flows: inferences from large-scale flume experiments. In: Shen, H.W. (Ed.), Hydraulic Engineering '93. American Society of Civil Engineers, New York, NY, pp. 1604–1609.

Iverson, R.M., Logan, M., Denlinger, R.P., 2004. Granular avalanches across irregular three-dimensional terrain: 2. Experimental tests. Journal of Geophysical Research 109, 49. https://doi.org/10.1029/2003JF000084.

Iverson, R.M., Logan, M., LaHusen, R.G., Berti, M., 2010. The perfect debris flow? Aggregated results from 28 large-scale experiments. Journal of Geophysical Research 115. doi:https://doi.org/10.1029/2009JF001514.

Debris-flow hazards and related phenomena. In: Jakob, M., Hungr, O. (Eds.), Springer Praxis Books. Praxis Publishing Ltd, Berlin, Heidelberg https://doi.org/10.1007/b138657.

Johnson, C.G., Kokelaar, B.P., Iverson, R.M., Logan, M., LaHusen, R.G., Gray, J.M.N.T., 2012. Grain-size segregation and levee formation in geophysical mass flows. Journal of Geophysical Research 117, n/a–n/a. doi:https://doi.org/10.1029/2011JF002185.

Kailey, P., 2013. In: University of Canterbury. Canterbury (Ed.), Debris Flows in New Zealand Alpine Catchments. UK PhD thesis.

Kailey, P., Bowman, E., Laue, J., Springman, S., 2011. Modelling debris flow processes with a geotechnical centrifuge. In: Italian Journal of Engineering Geology and Environment-Book (Ed.), 5th International Conference on Debris-flow Hazards Mitigation: Mechanics, Prediction and Assessment. Padua, Italy-14–17 June 2011, pp. 339–349 https://doi.org/10.4408/IJEGE.2011-03.B-039.

Kaitna, R., Hsu, L., Rickenmann, D., Dietrich, W., 2011. On the development of an unsaturated front of debris flows. In: Italian Journal of Engineering Geology and Environment-Book (Ed.), 5th International Conference on Debris-flow Hazards Mitigation: Mechanics, Prediction and Assessment. Padua, Italy-14–17 June 2011, pp. 351–358 https://doi.org/10.4408/IJEGE.2011-03.B-040.

Kattel, P., Khattri, K.B., Pokhrel, P.R., Kafle, J., Tuladhar, B.M., Pudasaini, S.P., 2016. Simulating glacial lake outburst floods with a two-phase mass flow model. Ann. Glaciol. 57, 349–358. https://doi.org/10.3189/2016AoG71A039.

Kattel, P., Kafle, J., Fischer, J.T., Mergili, M., Tuladhar, B.M., Pudasaini, S.P., 2018. Interaction of two-phase debris flow with obstacles. Eng. Geol. 242, 197–217. https://doi.org/10.1016/j.enggeo.2018.05.023.

Kean, J.W., McCoy, S.W., Tucker, G.E., Staley, D.M., Coe, J.A., 2013. Runoff–generated debris flows: observations and modeling of surge initiation, magnitude, and frequency. Journal of Geophysical Research: Earth Surface 118, 2190–2207. https://doi.org/10.1002/jgrf.20148.

Klute, A., Dirksen, C., 1990. Hydraulic conductivity and diffusivity: laboratory methods. In: Klute, A., Black, C.A. (Eds.), Methods of Soil Analysis. vol. 9(1). Amer. Soc. of Agronomy, Madison, Wisc., pp. 687–734.

Kowalski, J., McElwaine, J.N., 2013. Shallow two-component gravity-driven flows with vertical variation. J. Fluid Mech. 714, 434–462. https://doi.org/10.1017/jfm.2012.489.

Lanzoni, S., 1993. Meccanica di miscugli solido-liquido in regime granulo-inerziale. PhD thesis.

Lanzoni, S., Gregoretti, C., Stancanelli, L.M., 2017. Coarse–grained debris flow dynamics on erodible beds. Journal of Geophysical Research: Earth Surface 122, 592–614. https://doi.org/10.1002/2016JF004046.

Larcher, M., Fraccarollo, L., Armanini, A., Capart, H., 2007. Set of measurement data from flume experiments on steady uniform debris flows. J. Hydraul. Res. 45, 59–71. https://doi.org/10.1080/00221686.2007.9521833.

Legros, F., 2002. The mobility of long-runout landslides. Eng. Geol. 63, 301–331. https://doi.org/10.1016/S0013-7952(01)00090-4.

Lyu, L., Wang, Z., Cui, P., Xu, M., 2017. The role of bank erosion on the initiation and motion of gully debris flows. Geomorphology 285, 137–151. https://doi.org/10.1016/j.geomorph.2017.02.008.

Mainali, A., Rajaratnam, N., 1994. Experimental study of debris flows. J. Hydraul. Eng. 120, 104–123. https://doi.org/10.1061/(ASCE)0733-9429(1994)120:1(104).

Major, J.J., 1997. Depositional processes in large-scale debris-flow experiments. J. Geol. 105, 345–366.

Major, J.J., 1998. Pebble orientation on large, experimental debris-flow deposits. Sediment. Geol. 117, 151–164. https://doi.org/10.1016/S0037-0738(98)00014-1.

Major, J.J., 2000. Gravity-driven consolidation of granular slurries–implications for debris-flow deposition and deposit characteristics. J. Sediment. Res. 70.

McFall, B.C., Mohammed, F., Fritz, H.M., Liu, Y., 2018. Laboratory experiments on three-dimensional deformable granular landslides on planar and conical slopes. Landslides 15, 1713–1730. https://doi.org/10.1007/s10346-018-0984-2.

Mergili, M., Fischer, J.T., Krenn, J., Pudasaini, S.P., 2017. r. avaflow v1, an advanced open-source computational framework for the propagation and interaction of two-phase mass flows. Geosci. Model Dev. 10, 553–569. https://doi.org/10.5194/gmd-10-553-2017.

Mergili, M., Emmer, A., Juřicová, A., Cochachin, A., Fischer, J.T., Huggel, C., Pudasaini, S.P., 2018a. How well can we simulate complex hydro-geomorphic process chains? The 2012 multi-lake outburst flood in the Santa Cruz Valley (Cordillera Blanca, Perú). Earth Surf. Process. Landf. 43 (7), 1373–1389. https://doi.org/10.1002/esp.4318.

Mergili, M., Frank, B., Fischer, J.T., Huggel, C., Pudasaini, S.P., 2018b. Computational experiments on the 1962 and 1970 landslide events at Huascarán (Peru) with r.avaflow: lessons learned for predictive mass flow simulations. Geomorphology 322, 15–28. https://doi.org/10.1016/j.geomorph.2018.08.032.

Mergili, M., Jaboyedoff, M., Pullarello, J., Pudasaini, S.P., 2020. Back calculation of the 2017 Piz Cengalo-Bondo landslide cascade with r.avaflow: what we can do and what we can learn. Nat. Hazards Earth Syst. Sci. 20 (2), 505–520. https://doi.org/10.5194/nhess-20-505-2020.

Parsons, J.D., Whipple, K.X., Simoni, A., 2001. Experimental study of the grain-flow, fluid-mud transition in debris flows. The Journal of Geology 109, 427–447.

Pierson, T.C., 1986. Flow behavior of channelized debris flows, Mount St. Helens, Washington. In: Abrahams, A.D. (Ed.), Hillslope Processes. Allen & Unwin, Boston and London and Sydney. Binghamton's Symposia in Geomorphology International Series, pp. 269–296.

Pierson, T.C., 2005. Hyperconcentrated flow - transitional process between water flow and debris flow. In: Jakob, M., Hungr, O. (Eds.), Debris-flow Hazards and Related Phenomena. Praxis Publishing Ltd, Berlin, Heidelberg. Springer Praxis Books, pp. 159–202.

Pitman, E.B., Le, L., 2005. A two-fluid model for avalanche and debris flows. Philosophical Transactions. Series A, Mathematical, physical, and engineering sciences 363, 1573–1601. https://doi.org/10.1098/rsta.2005.1596.

Pudasaini, S.P., 2012. A general two-phase debris flow model. J. Geophys. Res. 117, F03010. https://doi.org/10.1029/2011JF002186.

Pudasaini, S.P., Domnik, B., 2009. Energy considerations in accelerating rapid shear granular flows. Nonlinear Process. Geophys. 16, 399–407. https://doi.org/10.5194/npg-16-399-2009.

Pudasaini, S.P., Fischer, J.T., 2020a. A mechanical erosion model for two-phase mass flows. Int. J. Multiphase Flow 132, 103416. https://doi.org/10.1016/j.ijmultiphaseflow.2020.103416.

Pudasaini, S.P., Fischer, J.T., 2020b. A mechanical model for phase separation in debris flow. Int. J. Multiphase Flow 129, 103292. https://doi.org/10.1016/j.ijmultiphaseflow.2020.103292.

Pudasaini, S.P., Hutter, K., 2007. Avalanche Dynamics: Dynamics of Rapid Flows of Dense Granular Avalanches. Springer-Verlag, Berlin, New York.

Pudasaini, S.P., Krautblatter, M., 2014. A two-phase mechanical model for rock-ice avalanches. Journal of Geophysical Research: Earth Surface 119, 2272–2290. https://doi.org/10.1002/2014JF003183.

Pudasaini, S.P., Mergili, M., 2019. A multi–phase mass flow model. Journal of Geophysical Research: Earth Surface 124, 2920–2942. https://doi.org/10.1029/2019JF005204.

Reid, M.E., Iverson, R.M., Logan, M., LaHusen, R.G., Godt, J.W., Griswold, J.P., 2011. Entrainment of bed sediment by debris flows: Results from large-scale experiments. In: Italian Journal of Engineering Geology and Environment-Book (Ed.), 5th International Conference on Debris-flow Hazards Mitigation: Mechanics, Prediction and Assessment. Padua, Italy-14–17 June 2011 https://doi.org/10.4408/IJEGE.2011-03.B-042.

Rondon, L., Pouliquen, O., Aussillous, P., 2011. Granular collapse in a fluid: role of the initial volume fraction. Phys. Fluids 23, 073301. https://doi.org/10.1063/1.3594200.

Sanvitale, N., Bowman, E.T., 2017. Visualization of dominant stress-transfer mechanisms in experimental debris flows of different particle-size distribution. Can. Geotech. J. 54, 258–269. https://doi.org/10.1139/cgj-2015-0532.

Sanvitale, N., Bowman, E., Genevois, R., 2011. Experimental measurements of velocity through granular-liquid flows. In: Italian Journal of Engineering Geology and Environment-Book (Ed.), 5th International Conference on Debris-flow Hazards Mitigation: Mechanics, Prediction and Assessment. Padua, Italy-14–17 June 2011, pp. 375–384 https://doi.org/10.4408/IJEGE.2011-03.B-043.

Savage, S.B., 1994. The mechanics of rapid granular flows. In: Mises, R.v., Dryden, H.L., Chernyi, G.G., Hutchinson, J.W., Yih, C.S. (Eds.), Advances in Applied Mechanics. Advances in Applied Mechanics vol. 24. Academic Press, Boston [etc.], pp. 289–366. https://doi.org/10.1016/S0065-2156(08)70047-4.

Savage, S.B., Hutter, K., 1989. The motion of a finite mass of granular material down a rough incline. J. Fluid Mech. 199, 177. https://doi.org/10.1017/S0022112089000340.

Scheidl, C., McArdell, B.W., Rickenmann, D., 2015. Debris-flow velocities and superelevation in a curved laboratory channel. Can. Geotech. J. 52, 305–317. https://doi.org/10.1139/cgj-2014-0081.

Stancanelli, L.M., Lanzoni, S., Foti, E., 2015. Propagation and deposition of stony debris flows at channel confluences. Water Resour. Res. 51, 5100–5116. https://doi.org/10.1002/2015WR017116.

Stiny, J., 1910. Die Muren: Versuch einer Monographie mit besonderer Berücksichtigung der Verhältnisse in den Tiroler Alpen. Wagner, Innsbruck.

Takahashi, T., 1983. Debris flow and debris flow position. In: Shahinpoor, M. (Ed.), Advances in the Mechanics and the Flow of Granular Materials. Trans Tech Publications, Clausthal-Zellerfeld a. o, pp. 55–77.

Takahashi, T., 1991. Debris flow. IAHR Monograph Series, Balkema, Rotterdam.

Takahashi, T., 2014. Debris Flow: Mechanics, Prediction, and Countermeasures. Second edition ed., CRC Press, Boca Raton, Florida. URL. http://search.ebscohost.com/login.aspx?direct=true&scope=site&db=nlebk&db=nlabk&AN=709475.

Tognacca, C., 1999. Beitrag zur Untersuchung der Entstehungsmechanismen von Murgängen. volume 164 of Mitteilungen/VAW, Versuchsanstalt für Wasserbau, Hydrologie und Glaziologie der Eidgenössischen Technischen Hochschule Zürich. Versuchsanstalt für Wasserbau Hydrologie und Glaziologie, Zürich.

Turnbull, B., Bowman, E.T., McElwaine, J.N., 2015. Debris flows: experiments and modelling. Comptes Rendus Physique 16, 86–96. https://doi.org/10.1016/j.crhy.2014.11.006.

van Steijn, H., Coutard, J.P., 1989. Laboratory experiments with small debris flows: physical properties related to sedimentary characteristics. Earth Surf. Process. Landf. 14, 587–596. https://doi.org/10.1002/esp.3290140614.

Sedimentation engineering. In: Vanoni, V.A. (Ed.), ASCE Manuals and Reports on Engineering Practice. Classic Ed.. vol. 54. ASCE American Society of Civil Engineers, Reston, Va

Varnes, D.J., 1978. Slope movement types and processes. In: Transportation Research Board (Ed.), Landslides: Analysis and Control. Transportation Research Board Special Report, pp. 11–33.

Wang, D., Chen, Z., He, S., Liu, Y., Tang, H., 2018. Measuring and estimating the impact pressure of debris flows on bridge piers based on large-scale laboratory experiments. Landslides 15, 1331–1345. https://doi.org/10.1007/s10346-018-0944-x.

Zanuttigh, B., Lamberti, A., 2007. Instability and surge development in debris flows. Reviews of Geophysics 45, n/a–n/a. doi:https://doi.org/10.1029/2005RG000175.

Zhou, G.G., Ng, C.W., 2010. Dimensional analysis of natural debris flows. Can. Geotech. J. 47, 719–729. https://doi.org/10.1139/T09-134.